ANALYSIS OF NEARLY SIMULTANEOUS X-RAY AND OPTICAL OBSERVATIONS OF ACTIVE GALACTIC NUCLEI

BY

JAMES RAYMOND WEBB

A DISSERTATION PRESENTED TO THE GRADUATE SCHOOL
OF THE UNIVERSITY OF FLORIDA IN PARTIAL FULFILLMENT
OF THE REQUIREMENTS FOR THE DEGREE OF
DOCTOR OF PHILOSOPHY

UNIVERSITY OF FLORIDA

1988

UNIVERSITY OF FLORIDA LIBRARIES

This work is dedicated to the memory of my father Joe Webb, my brother Daniel Joe Webb, and my grandmother Lema Webb. I learned so much from them all.

ACKNOWLEDGMENTS

The completion of this dissertation marks the attainment of a long-dreamed-of-goal. Many people have aided me in the pursuit of this goal, from fellow factory workers who listened to my tirades on black holes, to fellow students, to my family and loved ones who supported me emotionally for all of these years.

First and foremost, I would like to thank the person without whom this work still might be a dream: my wife Beatriz F. Fernandez. She helped me every step of the way, from data reduction in Boston to preparation of the final manuscript. She gave me encouragement when I had my doubts, calmed me when the computer gobbled my files, and most of all made me step away from this consuming task and live life. It is her love and understanding around which my world revolves.

So much of the credit for what I have achieved goes to my mother Inez E. Webb. She has supported me throughout this entire ordeal with the love and understanding only she could give. The poverty of graduate school and 2000 miles have kept us separated in space, but not in our hearts.

My sincerest thanks go to my adviser, Dr. Alex G. Smith. He gave me the opportunity to learn about quasars and to make contributions in the field. He patiently improved my confusing manuscripts and taught me how to communicate my ideas. His generous help has been invaluable during my years as a graduate student.

I would like to thank Dr Robert Leacock who was always there to find solutions to problems or just to listen to the rantings of a tired graduate student

I would also like to thank the members of my graduate committee, Dr James Hunter, Dr Heywood Smith, Dr James Ipser, Dr James Fry, and Dr Gary Ihas for their invaluable discussions on astronomy (and basketball) Dr Daniel Harris was extremely helpful and patient during my visit to SAO to reduce the x-ray observations

Thanks also go to Jeanne Kerrick and Hans Shreder who helped me with the details of graduate school I would like to thank all of my fellow graduate students to Joe Pollock who taught me the nuts and bolts of research and made me think about the details, To Andy Pica who, along with Jan, helped break me into the quasar program, to Greg Fitzgibbons, a fellow Hoosier, and Tom Barnello for their support and friendship during these years, to Billy Cooke who helped me with programming and generally made the office interesting and to my observing partners who had to put up with my lousy singing and powder sugar donuts, Paul Gombola, Mauricio Zitron, and Sandra Clemente

Special thanks go to Rafael and Luisa Fernandez for their generous and timely gift of the PC on which most of the analysis and word processing was done

TABLE OF CONTENTS

PAGE

ACKNOWLEDGEMENTS iii

LIST OF TABLES vii

LIST OF FIGURES ix

ABSTRACT xi

CHAPTER

I INTRODUCTION 1

- Research 1
- Nature of AGN 2

II OBSERVATIONS 5

- Source List 5
- Optical Data Reduction 7
- Optical Flux Conversion 11
- Conversion to Luminosity 11
- X-Ray data Acquisition 12
- The IPC Detector 13
- The HRI Detector 14
- X-Ray Flux Conversion 15
- Canonical Flux Conversion 17
- Spectral Indices 18
- IPC Errors 19
- HRI Errors 21
- Individual Sources 22
- Intrinsic Column Densities 44
- X-Ray Variability 46

III CORRELATIVE ANALYSIS 66

- Previous Studies 66
- Correlation Procedures 69
- Correlation Sample 74
- Flux Correlation Results 77
- Luminosity Correlations 93
- X-Ray Optical Spectral Indices 110
- Correlations with Luminosity Ratio 111
- The X-Ray Background 114
- Primary Conclusions from Correlations 115

PAGE

IV INDIVIDUAL SOURCE STUDY . . . 117

- Introduction . . . 117
- Synchrotron-Self-Compton Models . . . 118
- Multifrequency Observations . . . 126
- Conclusions . . . 151

V CONCLUSIONS . . . 153

BIBLIOGRAPHY . . . 157

APPENDIX . . . 162

LIST OF TABLES

TABLE		PAGE
1	CLOSEST X-RAY AND OPTICAL DATES	6
2.	X-RAY-OPTICAL TIME DELAYS	7
3.	AO 0235+164 X-RAY OBSERVATIONS	26
4.	3C 120 X-RAY OBSERVATIONS	27
5.	PKS 0735+17 X-RAY OBSERVATIONS	29
6.	OJ 287 X-RAY OBSERVATIONS	31
7.	3C 273 X-RAY OBSERVATIONS	33
8.	OQ 172 X-RAY OBSERVATIONS	34
9	AP LIB X-RAY OBSERVATIONS	35
10	3C 345 X-RAY OBSERVATIONS	36
11	3C 351 X-RAY OBSERVATIONS	37
12	1727+50 X-RAY OBSERVATIONS	38
13	PKS 2155-30 X-RAY OBSERVATIONS	41
14	X-RAY AND OPTICAL OBSERVATIONS	45
15	EXCESS COLUMN DENSITIES	48
16	X-RAY VARIABILITY	49
17	FLUX CORRELATIONS FOR ALL 70 OBSERVATIONS	80
18	FLUX CORRELATIONS	81
19	LUMINOSITY DATA	94
20	LUMINOSITY CORRELATIONS	98
21.	COMPARISON OF MEAN SPECTRAL INDICES	111
22	BEST FIT MODELS FOR 0235+164	142
23	MODELS FOR 0235+164	143

PAGE

24 BEST FIT MODELS FOR 0735+17 144
25 MODELS FOR 0735+17 144
26 BEST FIT MODELS FOR OJ 287 145
27 MODELS FOR OJ 287 146
28 BEST FIT MODELS FOR 3C 273 146
29 MODELS FOR 3C 273 147
30 BEST FIT MODELS FOR AP LIBRAE 148
31 MODELS FOR AP LIBRAE 149
32 BEST FIT MODELS FOR 3C 345 149
33 MODELS FOR 3C 345 150

LIST OF FIGURES

FIGURE PAGE

1 X-Ray Flux vs. Optical Flux All Observations 47

2 X-Ray and Optical Flux Curves of 0235+164 51

3 X-Ray and Optical Flux Curves of 3C 120 52

4 X-Ray and Optical Flux Curves of 0735+17 54

5 X-Ray and Optical Flux Curves of OJ 287 55

6 X-Ray and Optical Flux Curves of 3C 273 56

7 X-Ray and Optical Flux Curves of OQ 172 58

8 X-Ray and Optical Flux Curves of AP LIBRA 59

9 X-Ray and Optical Flux Curves of 3C 345 60

10 X-Ray and Optical Flux Curves of 3C 351 61

11 X-Ray and Optical Flux Curves of 1727+50 62

12 X-Ray and Optical Flux Curves of 2155-30 64

13 Flux Correlation Diagram ALL Observations 79

14 TDO Flux Correlation Diagram 84

15 TDWK Flux Correlation Diagram 84

16 TD2WK Flux Diagram 86

17 LACERTID Flux Diagram 86

18 QUASAR Flux Correlation Diagram 88

FIGURE PAGE

19. QUASAR+LACERTID Flux Correlation Diagram 88

20 BLAZAR Flux Correlation Diagram 90

21 OVV Flux Correlation Diagram 90

22 NON-OVV Flux Correlation Diagram 92

23 Luminosity Correlation Diagram ALL Observations 97

24 TDO Luminosity Correlation Diagram 100

25 TDWK Luminosity Correlation Diagram 100

26 TD2WK Luminosity Correlation Diagram 102

27. LACERTID Luminosity Diagram 102

28 QUASAR Luminosity Correlation Diagram 104

29 QUASAR+LACERTID Luminosity Correlation Diagram 104

30 BLAZAR Luminosity Correlation Diagram 108

31 OVV Luminosity Correlation Diagram 108

32 NON-OVV Luminosity Correlation Diagram 108

33 X-RAY-OPTICAL SLOPE VS REDSHIFT 113

34 SYNCHROTRON SPECTRUM 122

35 MULTIFREQUENCY SPECTRUM OF 0235+164 132

36 MULTIFREQUENCY SPECTRUM OF 0735+17 . 134

37 MULTIFREQUENCY SPECTRUM OF OJ 287 135

38 MULTIFREQUENCY SPECTRUM OF 3C 273. 137

39 MULTIFREQUENCY SPECTRUM OF AP LIBRAE 139

40 MULTIFREQUENCY SPECTRUM OF 3C 345 140

Abstract of Dissertation Presented to the Graduate School
of the University of Florida in Partial Fulfillment of the
Requirements for the Degree of Doctor of Philosophy

ANALYSIS OF NEARLY SIMULTANEOUS X-RAY AND OPTICAL OBSERVATIONS OF ACTIVE GALACTIC NUCLEI

By

James Raymond Webb

August 1988

Chairman: Alex G. Smith
Major Department: Astronomy

Rosemary Hill optical and EINSTEIN X-ray observations of a sample of 36 active galactic nuclei (AGN) were reduced and analyzed. Seventy-two x-ray observations of these sources were reduced, nineteen of which yielded spectral information. Of these spectral observations, significant hydrogen column densities above the galactic value were required for nine of the active galactic nuclei. X-ray variability was detected in eight of the eleven sources which were observed more than once by EINSTEIN.

Correlations between the x-ray and optical luminosities were investigated using the Jefferys method of least squares. This method allows for errors in both variables. The results indicate a strong correlation between the x-ray and optical luminosities for the entire sample. Division of the sample into groups with similar optical

variability characteristics show that the less violently violent variable AGN are more highly correlated than the violently variable blazars.

Infrared and radio observations were combined with the x-ray and optical observations of six AGN. These sources were modelled in terms of the synchrotron self-Compton model. The turnover frequency falls between the infrared and radio data and reliable estimates of this parameter are difficult to estimate. Therefore the results were found as a function of the turnover frequency. Four sources required relativistic bulk motion or beaming. Multifrequency spectra made at different times for one individual source, 0235+164, required different amounts of beaming to satisfy the x-ray observations. Sizes of the emitting regions for the sources modelled ranged from 0.5 parsec to 1.0 parsec.

CHAPTER I
INTRODUCTION

Research

The study of Active Galactic Nuclei (AGN) has made significant progress in the last ten years, primarily due to the advent of x-ray astronomy. The x-ray observations of AGN combined with ultraviolet, optical, infrared and radio observations have given researchers multi-frequency spectra extending over ten decades in frequency. The problem with most observations covering several frequency bands is non-simultaneity. Most AGN are variable in every frequency band observed, so multi-frequency observations must be made as nearly simultaneously as possible. Simultaneous observations are notoriously difficult to obtain because each frequency band requires different instruments, some of these being heavily scheduled satellite-based telescopes.

In this research we have combined optical observations of AGN made with the 76-cm reflecting telescope at Rosemary Hill observatory (RHO) with x-ray observations from the EINSTEIN x-ray observatory. We have attempted to assemble a set of nearly simultaneous x ray and optical observations and to examine this data for clues regarding the nature of the emission mechanisms responsible for the radiation.

One approach is to look at all the sources simultaneously and perform correlation analyses using the x-ray and optical fluxes. This approach was taken in Chapter III. An alternative approach is to look at individual objects and model their multifrequency spectra. The results of this approach are described in Chapter IV.

Chapter II describes the data reduction procedures used to reduce the optical and x-ray observations. This detailed account is important because great care was taken to reduce the optical and x-ray observations consistently. Also in Chapter II, the individual objects are described and variability is discussed. Chapter V contains the basic conclusions of this research and suggests directions for further study.

Nature of AGN

The class of extragalactic sources commonly called "AGN" usually includes quasars, BL Lacertae objects, N galaxies, and Seyfert galaxies. Nearly all AGN exhibit power-law optical continua and all probably emit x-rays at some intensity level.

Quasars are distinguished by their broad, redshifted emission lines superimposed on the underlying power-law continuum. About ten percent of all quasars are strong radio sources, the remaining quasars are as yet undetected in the radio band. The radio-loud quasars usually exhibit large amplitude optical variability while the radio-quiet group exhibit only modest optical variability. A radio luminosity of 10^{41} ergs/sec is the dividing point usually used to distinguish between radio-loud and radio-quiet quasars (Ku, Helfand and Lucy 1980). Most quasars observed have been detected as x-ray sources regardless of their radio properties.

BL Lacertae objects exhibit many of the same properties as radio-loud quasars, with the notable exception that they lack broad emission lines. BL Lac sources have highly polarized optical continua and show extremely rapid, high amplitude optical variations. Although emission lines are rarely detected, many BL Lacs have absorption lines in their optical spectra from which redshifts can be obtained. Recently some faint emission systems have been identified in a few BL Lacs; the redshifts of these lines are larger than those of the absorption line systems.

The N-galaxies and Seyfert galaxies resemble normal elliptical and spiral galaxies, respectively, but have bright, quasar-like nuclei. These bright nuclei tend to be intrinsically fainter than the classical quasars and are usually associated with strong, compact radio sources. The resemblance that the outer regions of N-type and Seyfert galaxies bear to normal galaxies and that their bright nuclei bear to quasars suggests an evolutionary sequence between normal galaxies and quasars. Imaging studies of several quasars have shown that nearby quasars are imbedded in nebulosity with spectral properties resembling young galaxies (Boroson, Oke, and Green 1982). This evidence further strengthens the case for an evolutionary connection between AGN and normal galaxies.

The evidence that all AGN have similar nuclear components becomes more convincing as more sensitive observations of various types of sources are made. The most popular model for the compact cores of AGN consists of a supermassive black hole accreting matter from a disk, converting a large percentage of this accreted mass into energy. The gravitational energy of the infalling particles is converted into radiation, most of which escapes along the spin axis of the black hole

Presumably, magnetic fields aligned parallel to the rotational axis of the hole are associated with both the hole and the disk. Particle acceleration, synchrotron emission, and photon-particle interactions in the escape funnel are most likely responsible for the power law continuum seen in AGN (Blandford and Znajek 1977). Massive black hole models were created to account for the large energy budget of the central core of AGN. If one interprets the large redshifts measured from emission lines as non-cosmological in origin, quasars could then be local and the luminosities would be considerably reduced. Halton Arp and others have suggested such models on the basis of peculiar quasar-galaxy apparent positional associations (Burbidge 1980; Arp 1987). Although this evidence is interesting, it is not compelling; the bulk of evidence favors the cosmological interpretation of quasar redshifts. The lack of blue shifts, the measurement of similar redshifts for the fuzz surrounding nearby AGN, and the continuity of properties from active galaxies through quasars all provide convincing evidence that the redshifts are properly interpreted as indicators of distance through Hubble's relation (Weedman 1986). In this research we will use the measured redshifts as indicative of the distances to the AGN.

CHAPTER II
OBSERVATIONS

Source List

All of the AGNs analyzed in this work were observed at Rosemary Hill Observatory (RHO) in the optical spectral band and with the EINSTEIN x-ray telescope. These sources were chosen by comparing the RHO master list with the third edition EINSTEIN observing catalog. The reliability of optical calibrations was a further restriction. Only EINSTEIN Imaging Proportional Counter (IPC) and High Resolution Imager (HRI) observations were used because both detectors have similar frequency responses and are reliably calibrated. These restrictions, although limiting the number of sources involved, assured the data could be consistently reduced and compared.

Table 1 lists the thirty-six sources selected for this study. Column 1 gives the source name, column 2 the adopted redshift, column 3 the source type, and columns 4 and 5 list the dates the x-ray and optical observations were made respectively. Emission line redshifts were used whenever available and the presence of dashes in column 2 indicates that no redshift is known for that source. Some sources were observed more than once with the EINSTEIN observatory.

TABLE 1.

CLOSEST X-RAY AND OPTICAL DATES

SOURCE NAME	REDSHIFT	TYPE	X-RAY DATE	OPTICAL DATE
0007+12	0.089	SEY	12/19/80	12/05/80
0035+12	---	LAC	1/02/80	1/08/80
3C 66A	0.444*	LAC	7/23/80	7/23/80
0235+164	0.940	LAC	7/22/80	7/22/80
0420-01	1.740	QSO	3/06/80	3/06/80
3C 120	0.033	SEY	9/06/79	9/19/79
NRAO 190	0.850	QSO	6/06/80	3/06/80
0735+17	0.420	LAC	10/09/80	10/09/80
OI 363	0.630	QSO	10/26/79	10/22/79
OI 090.4	---	LAC	4/27/79	4/21/79
0846+51	1.860	LAC	5/02/80	3/15/80
OJ 287	0.306	LAC	4/14/80	4/17/80
0906+01	1.018	QSO	5/19/79	5/27/79
MRK 421	0.031	ELL	11/20/79	11/17/79
3C 273	0.158	QSO	6/20/79	6/20/79
1308+32	0.996	LAC	6/30/80	7/04/80
OQ 172	3.530	QSO	7/29/79	7/26/79
1510-08	0.340	QSO	2/10/80	2/18/80
AP LIB	0.049	LAC	2/10/81	2/11/81
1538+14	---	LAC	8/07/80	8/01/80
3C 345	0.595	QSO	8/27/79	8/15/79
3C 351	0.371	QSO	7/25/79	7/28/79
1727+50	0.055	LAC	7/25/79	7/26/79
1749+09	---	QSO	10/08/80	10/08/80
1749+70	---	LAC	7/22/79	7/22/79
3C 371	0.052	LAC	7/21/79	7/21/79
OV 236	0.353	QSO	10/17/79	10/17/79
2128-12	0.501	QSO	5/10/80	5/20/80
2135-14	0.200	QSO	5/10/80	5/11/80
2155-30	0.117	LAC	11/05/79	11/05/79
2200+42	0.068	LAC	6/08/80	6/08/80
2201+31	0.297	QSO	6/15/80	6/15/80
2216-03	0.901	QSO	5/24/79	5/30/79
3C 446	1.404	QSO	6/09/80	6/11/80
2230+11	1.030	QSO	11/24/79	11/16/79
2345-16	0.600	QSO	12/05/79	11/15/79

Table 2 lists these sources along with the number of available x-ray observations for each source. The time between the x-ray and optical observations in days is given in column 3. A comparison of the x-ray and optical variability characteristics of these sources is presented later in this chapter.

TABLE 2.
X-RAY-OPTICAL TIME DELAYS

SOURCE NAME	# OF X-RAY OBSERVATIONS	DELTA T (DAYS)
0235+164	6	0,3,4,14,15,20
3C 120	5	14,18,20,30,34
0735+17	5	0,0,9,12,20
OJ 287	2	2,150
3C 273	4	0,3,21,23
OQ 172	2	3,4
AP LIB	4	1,4,8,30
3C 345	4	12,17,60,78
3C 351	8	3,3,6,8,11, 70,70,73
1727+50	2	1,2
2155-30	3	0,13,62

Optical Data Reduction

The optical observations were made with the 76-cm reflecting telescope at RHO. Photographic photometry was done at the f/4 Newtonian focus using hypersensitized Kodak 103a-O emulsions. The plates were hypersensitized by nitrogen baking, followed by hydrogen soaking. The hypersensitized plates were stored at a temperature of -20 degrees Centigrade in an atmosphere of dry nitrogen until needed at the telescope. The plates were then warmed, loaded into nitrogen pressurized cassettes equipped with filter windows, and finally exposed at the telescope. The plates were promptly developed and measured using a Cuffey variable iris photometer.

The diameter and optical density of each quasar image was measured along with those of ten or more standard stars within 20 arc minutes of the source image. The standard stars were non-variable stars whose brightnesses were accurately known. Calibrations of these comparison stars have been obtained from the literature or calibrated at Rosemary Hill by photographic transfer from a field which contains photoelectric standards. Many RHO observers have contributed to the compilation of calibration sequences throughout the 20-year history of the monitoring program. Magnitudes for the AGN's were obtained by fitting a parabolic calibration curve to the iris readings and magnitudes of standard stars (Pica 1982).

Magnitude errors were estimated from the RMS deviation of the standard stars around the calibration curve. This error evaluation procedure has recently been re-examined and found to be an accurate estimation of errors by Pica *et al.* (1987).

Some sources were observed in the international photographic system (PG) and others in the Johnson B color system. Conversion of the PG observations to B magnitudes was done following Lu (1972) and involved empirical corrections based on the U-B color of the sources.

Before magnitudes can be converted to flux incident on our galaxy, galactic absorption and emission line contributions must be taken into account. The emission line corrections were calculated by the method of Schmidt (1968) which is shown in equation (2-1).

$$M = \frac{\int E(v) \times S(v)\, dv}{\int S(v)\, dv} \qquad (2\text{-}1)$$

The v's in equation (2-1) represent frequency. The transmission function S(v) for the B color system was tabulated by Matthews and

Sandage (1963) and the equivalent widths of the emission lines E(v) were obtained from Pica (1982) and Hewitt and Burbidge (1987).

In an effort to reduce the optical and x-ray data consistently, the previously used sec(z) law of galactic extinction has been abandoned in favor of a new method utilizing neutral hydrogen observations. Reddening values were obtained for each source from the neutral hydrogen and galaxy count studies of Burstein and Heiles (1982). Their reddening values account for the variable gas-to dust ratios seen in different directions of the Galaxy and provide reddening to an accuracy of 0.01 magnitude. The B-band extinction was calculated from the reddening value following the work of Seaton (1979). He gives the extinction in magnitudes as

$$A_B = 4.16556 \times E(B-V) \qquad (2\text{-}2)$$

Differences between the extinction calculated by the sec(z) law and the method outlined above as large as 0.6 magnitude were found, but in the majority of cases the differences were less than 0.2 magnitude.

In some cases the x-ray observations indicated a significant hydrogen column density in excess of that measured in the neutral hydrogen surveys. This excess column density is presumably intrinsic to the AGN. The extinction of the optical continuum flux can be computed from the excess column density using the expressions relating the hydrogen column density to reddening from Burstein and Heiles (1978), and equation (2-2). Equation 7 in Burstein and Heiles assumes a constant gas-to-dust ratio and is

$$E(B-V) = -0.055 + 0.000443 \times Nh' \qquad (2\text{-}3)$$

$$Nh' = Nh / 2.23 \times 10^{18} \qquad (2\text{-}4)$$

Once the intrinsic reddening was calculated, the B band intrinsic absorption was determined from equation (2-2). The E(B-V) values for two sources, BL Lac and AO 0235+164, were unreasonably high with E(B-V)'s in excess of 1.0, resulting in four magnitudes of intrinsic extinction in these high luminosity sources. When the optical fluxes were calculated using these intrinsic absorption values, the flux increased so that points on a graph of log(Fx) vs. log(Fo) fell well outside the range seen in other sources. This alone implied an unrealistic assumption in determining the optical extinction. Before rejecting or revising this method for calculating the intrinsic extinction, we examined other methods for determining intrinsic or intervening reddening. Calculations of reddening from emission line studies of AGN indicate the intrinsic reddenings of all AGN is between 0.00 and 0.50 (MacAlpine 1985). Actual emission line studies for the sources with intrinsic reddening in this study were impossible because of the lack of emission lines in these BL Lac sources. We chose to scale the highest intrinsic E(B-V) found in our x-ray observations down to the observed limit of 0.5. This scaling resulted in more reasonable optical fluxes for the three sources where intrinsic hydrogen column densities were indicated by the x-ray spectra.

A possible explanation for the excessive extinction determined from the x-ray column density (eq. 2-3) is that the gas-to-dust ratio in these sources is probably different from the galactic value on which equation (2-3) is based. Also, MacAlpine suggests that the extinction properties of the dust in AGN may differ from those of galactic dust. The validity of either of these suggestions is uncertain, the scaling remains an assumption based primarily on the emission line studies.

Optical Flux Conversion

The corrected magnitudes were converted to monochromatic flux at 4409 A by:

$$f(\text{obs}) = 4.44 \times 10^{(15.0-M)/2.5} \qquad (2\text{-}5)$$

The flux f(obs) is in units of millijanskys, and the constants were taken from the work of Johnson (1966). We converted to the source rest frame at 2500 A using equation (2-6)

$$f(\text{ss}) = \left[\frac{2500\ (1+z)}{4409}\right]^{\alpha} (1+z)^{-1}\ f(\text{obs}) \qquad (2\text{-}6)$$

In equation (2-6), α is the optical spectral index and z is the redshift. The spectral index for each source was calculated by fitting a least squares line to U-B and B-V data from Hewitt and Burbidge (1987). The power law assumption is a close approximation over the limited frequency range involved here.

Conversion to Luminosity

In order to compute a luminosity in the rest frame of the source, we must assume a cosmological model and an interpretation for the redshift. As discussed in the introduction, we assumed the measured redshifts of spectral lines (emission lines when available) are cosmological shifts and indicate the distance to the source. We further assumed a Friedmann cosmology with the luminosity distance given by equation (2-7)

$$A = q_0^{-1}z + q_0^{-2}(q_0 - 1)[(1 + 2q_0z)^{0.5} - 1] \qquad (2\text{-}7)$$

A deceleration parameter of $q_0 = 0.0$ reduces the luminosity distance to

$$A = z(1 + z/2) \qquad (2\text{-}8)$$

The luminosity is then related to the flux by equation (2-9)

$$L(2500) = \left[\frac{4\pi c^2}{H_0^2}\right] A^2 f(em) \frac{\text{ergs}}{\text{sec-Hz}} \qquad (2\text{-}9)$$

These luminosity conversion equations are equally valid for the x-ray observations and will be used throughout this work. Tests using different values of q_0 and H_0 (Webb 1985) indicate specific choices of these parameters do not significantly alter correlative results. In view of this, we examined only the case with $q_0 = 0.0$ and $H_0 = 55$ km/Mpc sec.

X-ray Data Acquisition

The x-ray observations analyzed in this research were all made with the EINSTEIN x ray observatory. The HEAO 2 satellite was launched in

1978 and was in operation until late 1981. The telescope consisted of a high resolution mirror, several instruments which were rotated into the mirror focal plane, and several gratings and filters which could be introduced into the light path. Three image dissector star trackers determined the telescope orientation with an accuracy of one minute of arc.

The high resolution mirror was based on Wolter type 1 geometry, i. e. a paraboloidal element and a confocal, coaxial hyperboloidal element. The EINSTEIN mirror consisted of four nested paraboloid-hyperboloid surfaces which focused grazing incidence x-ray photons in the focal plane. The plate scale at the focal plane was 1 mm/arcsec. The effective area of the mirror varied between 400 square centimeters at 0.25 KeV and 30 square centimeters at 4 KeV. Further details about the mirror are published in Van Speybroeck (1977).

The focal plane instruments which are of interest here are the imaging proportional counter (IPC) and the high resolution imager (HRI). The two instruments are briefly described in the next two sections.

The IPC Detector

The IPC detector was a gas proportional counter filled with a pressurized, density regulated mixture of argon, xenon and CO_2. Two planes of cathode wires were sandwiched around a single plane of anode wires. An electrical potential difference was maintained between the anode and cathode wires. The wire spacing determined the resolution of the IPC. The spacing of the cathode wires (1 mm) set the accuracy in the spatial coordinate at one arcminute. Incident x-ray photons produced cascades in both cathode wires, and the associated pulse height electronics determined both the location and the energy of the photons. Technical parameters and performance characteristics can be found in Schrier (1978), Giacconi et al. (1979) and Gorenstein et al. (1978). The uncertainties in flux measurements at first processing were estimated at thirty percent of the measured flux. The primary uncertainty was the gain variation due to a faulty gas pressure valve. The reprocessing of all IPC data reduced the flux uncertainty. Madejski and Schwartz (1988) estimated the flux uncertainty for high count rate observations of OJ 287 and PKS 0735+178 as 6%. They remarked that the primary cause of uncertainty is the gain variation. In low count observations, however, other factors such as quantization of energy channels and uncertainty in detector on/off times lead to larger errors in flux estimation. The IPC errors will be discussed in a later section.

The HRI Detector

The HRI was a multi-channel plate detector consisting of two layers of tubes separated by 38 microns. The x-rays reflected from the mirror at an angle between 5 and 2.5 degrees. They struck the first multi-channel plate, whose entrance face was coated to enhance photoelectron production. The photoelectrons cascaded through the first plate and into the second plate, where the channel tubes were inclined by six degrees. The separation between the two channel plates allowed the photoelectrons from the first stage to be spread over several second stage channel tubes. The photoelectrons emerging from the second channel plate struck an anode grid which was connected to amplifiers. These amplifiers determined the position and energy of the initial x ray. Technical information on the design and performance of the HRI can be found in Kellogg, Henry, Murray and Van Speybroeck (1976).

The HRI had very little energy resolution and was used primarily for obtaining high quality x ray maps. The broad band HRI flux was used in this research to complement the IPC observations. In order to calculate the flux, spectral parameters must be assumed. Since we had IPC observations for all of the sources which have HRI observations the spectral and column density parameters derived from the IPC spectra were used to calculate the HRI flux.

X-ray Flux Conversion

The primary reduction of the x-ray observations was done at the Harvard-Smithsonian Center for Astrophysics (CFA) in Cambridge, Massachusetts. The facilities at CFA included sophisticated programs which processed the original pulse height data according to the specifications of the detectors. Second level programs fitted model spectral distributions to the photon count data using the energy index and the hydrogen column density as adjustable fitting parameters. The broad band fluxes were then computed using the "best fit" parameters determined by a chi-square minimization algorithm. Equation (2-10) shows the dependance of the measured flux on various parameters determined from the count data and the minimization program.

$$S(E_1,E_2) = \frac{N_c(E_1,E_2)\int \exp[-\sigma(E) \times Nh] \times E^{1-\beta}\, dE}{T \int A(E) \times \exp[-\sigma(E) \times Nh] \times E^{\beta}\, dE} \qquad (2\text{-}10)$$

The net counts between energies E_1 and E_2 are represented by $N_c(E_1,E_2)$, and T is the effective exposure time. The cross-section for neutral hydrogen is $\sigma(E)$, the hydrogen column density is Nh, and the detector response function is A(E). All spectral fits were power laws where β is the photon energy index.

The nine channels between 0.42 and 4.33 KeV were typically used to fit the spectrum because these channels usually had a larger signal to noise ratio than the other three channels. The flux was calculated between 0.5 and 4.0 KeV. In some cases the count rate was too low to allow reliable determination of the spectral parameters. In these cases, the canonical value of 1.7 was used for the photon spectral index and the measured galactic hydrogen column density was used in equation (2-10). In cases where several x-ray observations of the same source were available, the high count rate observations were used to determine the spectral parameters and the other observations were reduced using these parameters.

Once the broad-band flux was determined, the monochromatic flux at 2 KeV was calculated by the following equations. The definition of broadband flux is

$$F(0.5\text{-}4.5) = \int F(\nu)^{\alpha}\, d\nu \qquad (2\text{-}11)$$

In equation (2-11), the $F(\nu)$ is the flux at frequency ν and is integrated between the limits corresponding to 0.5 and 4.5 KeV. We assumed the flux is a power law in frequency with index α_x, so equation (2-11) becomes:

$$K = \frac{F(0.5-4.5)}{\int \nu^{-\alpha_x} d\nu} \qquad (2\text{-}12)$$

The constant K was then used to find the flux at 2 KeV by substituting into equation (2-13).

$$F(2\ \mathrm{KeV}) = K \times \nu(2\ \mathrm{KeV})^{-\alpha_x} \qquad (2\text{-}13)$$

The spectral index, α_x, is important in the determination of the monochromatic flux but cannot be determined in some of the x-ray observations. When no spectral index was available from the spectral fit, the canonical spectral index was assumed.

Canonical X-ray Spectrum

The early x-ray spectral observations of AGN were consistent with power law spectral distributions with an index of 0.7+/-0.1 (Mushotzky *et al.* 1980, Mushotzky and Marshall 1980, and Mushotzky 1982). The universal slope seemed to be a good approximation of the spectral index of all AGN, regardless of intrinsic luminosity. Later EINSTEIN observations seemed to confirm this "universal" spectral index. The "universal" spectral index was shown to be too simplistic when a number of other quasars, specifically radio-quiet quasars, were analyzed. Wilkes and Elvis (1986) reported that the soft x-ray slopes of 30 quasars suggested a diversity of x-ray spectral indices. Elvis and

Lawrence (1985) showed that the x-ray spectral indices of some sources are as large as 2.2.

Obviously the best way to determine the x-ray spectral index for an individual source is to observe the x-ray spectrum and fit a power law distribution to the data. Many observations had such low count rates that little if any spectral information was available. In these cases, the x-ray flux was computed using the canonical spectral index of 0.7. This is the only viable approximation possible until longer and more sensitive observations of these sources can be made.

The lack of spectral information also prevented independent determination of the hydrogen column density. In cases where the "canonical" or "universal" spectral index was used, we also assumed a column density equal to the measured galactic value in the direction of the source.

Spectral Indices

Several types of spectral indices are used in x-ray astronomy. The first type, encountered in equation (2-10), is called the photon energy index. This index is the slope of a power law fit to the count data per energy bin. The symbol for the photon energy index is β (see eq. 2-10). Another index, usually called the x-ray spectral index, relates the log of the x-ray flux to the log of the frequency at which the flux is measured. The photon energy index is simply 1.0 larger than the x-ray spectral index. The x-ray spectral index is usually denoted by α_x and is the one discussed in the canonical x-ray spectrum section.

General spectral indices between two frequency bands, 1 and 2, are defined by equation (2-14)

$$\alpha_{12} = \frac{\log(F_2/F_1)}{\log(\nu_2/\nu_1)} \tag{2-14}$$

The F_i's represent the fluxes in each frequency band and the ν's are the frequency band centers. These spectral indices are commonly used in multifrequency studies.

IPC Errors

Uncertainties are present in the calculation of both the flux and the spectral parameters of a specific x-ray observation. The following discussion was taken primarily from Madejski and Schwartz (1988).

Flux Determination Uncertainties

The major source of systematic error in converting from count rates to flux is the detector gain, which is modeled by adding two sources of error in quadrature. The first part is a purely spatial term that is due to the non-uniformity of the anode wire separations. In the central part of the IPC detector (where most of the observations analyzed here were made) the gain was well calibrated. The RMS dispersion of the gain (in units called BAL, which were determined from a calibration source) is 0.15 in this calibrated area. If the source was poorly centered, the x-rays would fall outside of the central region of the detector, where the RMS dispersion is 0.6 BAL.

The second source of error is from a purely temporal term that arises from the time variation of gas pressure in the detector vessel. The pressure was closely monitored in flight and is known to a precision of 0.15 BAL (Madejski and Schwartz 1988). For observations made within the central calibrated region, the total uncertainty is 0.21 BAL, while observations made outside this region have uncertainties of 0.61 BAL. We followed Madejski and Schwartz in estimating the uncertainties in all observations as 0.6 BAL, regardless of the distance off axis.

The flux determined from best fit spectral parameters varies by about 4% as the gain varies by 0.6 BAL. Other sources of error can add an additional 4% uncertainty (again added in quadrature), so the total systematic error is roughly 6%.

The count rate statistics also adds uncertainty to the flux estimate. This statistical uncertainty was added to the total systematic error in quadrature to determine the total uncertainty in the flux observations.

Spectral Parameters

Madejski and Schwartz (1988) also found that gain variations of 0.2 BAL caused variations of 0.1 in both the photon index and the log of the column density of 0.1. A gain variation of 0.6 BAL caused variations in the spectral parameters of 0.25. These uncertainties represent systematic errors in the spectral parameters for observations made inside and outside the well calibrated regions of the detector, respectively.

The statistical error in the spectral parameters due to uncertainties in the fitting scheme was examined by Avni (1976). The 90% confidence region in either parameter is found by adding 4.6 to the minimum chi-square value and then finding the chi-square contour of this value. The 4.6 is for a model with two fitted parameters. Although the software which produces the contour diagrams was not available, the uncertainties in the spectral parameters were estimated by interpolation of the chi-square tables in the IPC output. These interpolated uncertainties are quoted in parentheses with the spectral parameters in the following sections.

HRI Errors

Since the HRI instrument was primarily an imaging device, the uncertainties in determining the flux were not as well studied. The total HRI uncertainty is defined as the sum of the 5% systematic error and the count rate uncertainty added in quadrature. This error was used because of the lack of any other acceptable method of calculating the HRI uncertainty. A total of six HRI observations was used and they were carefully examined for consistency with the IPC results. Only one HRI observation, an observation of 3C 351, gave a flux significantly different from the IPC observations. This observation is discussed in the subsection devoted to 3C 351.

Individual Sources

The x-ray and optical observations of each source are described in the following sub-sections. The sources are listed in right ascension order. All references to emission lines and emission line widths are from Pica (1985) unless stated otherwise. Similarly, all redshift references are from Hewitt and Burbidge (1987) and all galactic hydrogen column densities are from Stark et al. (1988). The E(B-V) values for all sources were taken from Burstein and Heiles (1982). All flux densities at 2 KeV have units of ergs/cm^2-sec-Hz unless stated otherwise.

The individual x-ray observations are identified by their sequence number which refers to the EINSTEIN fourth edition catalog. An H after this sequence number indicates the observation was made with the high resolution imager (HRI) rather than the IPC. All observations without this indicator were made with the IPC detector.

0007+10

The Seyfert galaxy 0007+10, commonly referred to as IIIZW-2, has a measured redshift of z = 0.089. This optically active source has been observed regularly from RHO since 1978. The optical observations of 0007+10 were corrected for hydrogen emission lines at 5102, 4861, 4340 and 4102 angstroms. The resulting continuum magnitude was then corrected for galactic extinction of 0.12 magnitude and 0.47 magnitude of intrinsic extinction. An optical spectral index of 1.75 was used to calculate the flux from the magnitude values.

The optical observation made on the night of 12/05/80 was the closest optical measurement to the EINSTEIN x-ray observation of 12/19/80. An inspection of the optical light curve around that date showed IIIZW-2 near its mean brightness level. It experienced a long term decline through 1979 and most of 1980, from a maximum brightness of B = 14.3 in late 1978. Subsequent observations showed a 0.8 magnitude flickering around B = 15.5 for the next 3 years.

The x-ray observation, with an effective exposure time of 3.7 hours, registered 362 counts between 0.5 and 4.5 KeV. The count rate was sufficient to estimate the spectral index and hydrogen column density. The best fit power law was characterized by an x-ray spectral index of 1.5(0.5) and a column density of 3.162(1.0) x 10^{21} atoms/cm^2. The numbers in parentheses are 90% confidence uncertainties. The 2 KeV flux density incident on our galaxy calculated from the best fit spectral parameters was 3.17(0.27) x 10^{-30} ergs/cm^2 sec Hz. Appendix 1 contains plots of the power-law fits to the count data for all observations used to obtain spectral parameters for this and all other sources.

The measured hydrogen column density in our galaxy (Stark _et al._ 1988) was smaller than the column density determined from the x-ray spectrum. The discrepancy in the column densities is taken here to indicate column density intrinsic to the source or between our galaxy and the source.

0035+12

This source is a BL Lacertae type object which has no measured redshift. The x-ray observation was made on 1/2/80 and the object was photographed six days later on 1/8/80 from Rosemary Hill. Unfortunately, a relatively short x-ray exposure time (1.7 hours) resulted in a small number of counts (19+/-6). Since no spectral information was available, the canonical spectral index of 0.7 and the galactic column density were used to calculate the x-ray flux. The monochromatic flux density at 2 KeV was 1.9(.58) x 10^{-31} ergs/cm^2-sec-Hz.

3C 66A

This strong radio source is a BL Lac with a measured redshift of 0.444. The only measured emission line is at 2798 angstroms. This source has been monitored at RHO since 1978, and the exposure on 7/23/80 was made only hours before the x-ray observation.

The 5.5 hour x-ray observation yielded 215 counts, and the power law fit gave a spectral index of 1.6(0.6). The hydrogen column density was found to be greater than the galactic value measured in the direction of the source. The resulting x-ray flux density was 1.43(0.14) x 10^{-30} ergs/cm^2-sec-Hz. The optical flux was calculated with an optical spectral index of 1.4, and an extinction of 0.58 magnitude was used as a result of both galactic and intrinsic extinction.

0235+164

Optically violent variable AO 0235+164 is a Lacertid with an emission line redshift of 0.94 (Hewitt and Burbidge 1987). It exhibits a steep optical spectrum with an index around 3.0. The optical continuum is highly polarized. This object has been monitored optically at RHO since December of 1975 at a rate of about two observations per week during its observing season.

A number of observations of 0235+164 were made with the EINSTEIN x-ray observatory, and six of these observations were analyzed for this research. All of the observations were made with the IPC, and spectral information from the independent fits showed a large range in spectral indices. Hereafter, all observations are referred to by their sequence number which denotes their order in the EINSTEIN 4th edition observing catalog. Observations 9562 and 9285, were made only one day apart, but the spectral indices differed by 1.5. Since this disparity of spectral indices is not likely to be real, only observation 9285 was used to determine the spectral index and hydrogen column density. This observation was chosen because of the low chi-square of the spectral fit. The spectral parameters found from this fit were used to reduce all of the other 0235+164 x-ray observations as well.

The best fit power law to observation 9285 had a slope of 1.6(0.2) and required a hydrogen column density in excess of the measured galactic value for that direction. Extinction due to both galactic and intrinsic dust of 1.8 magnitudes was used to correct the optical magnitudes. Table 3 gives the Julian date and flux for each observation of 0235+164. Column 1 of Table 3 lists the Julian date of the beginning of the x-ray observation and Column 2 gives the sequence number of the observation. Column 3 contains the 2 KeV flux density with the total error in parentheses. Column 4 lists the delay time (DT) between the x-ray and optical observation in days. Columns 5 and 6 give the total counts and the live time (in seconds) of the observation.

TABLE 3.
AO 0235+164 X-RAY OBSERVATIONS

J.D. (-2,400,000)	SEQ #	FLUX DENSITY ($\times 10^{-30}$)	DT (DAYS)	COUNTS	LIVE TIME
44442	5691	2.24(0.37)	7.0	58.1	1566.6
44629	7506	1.73(0.26)	20.0	83.1	4340.9
44442	7507	3.66(0.50)	0.0	84.1	2019.4
44274	9283	2.89(0.65)	4.0	30.9	1480.3
44442	9285	4.01(0.31)	14.0	556.9	11872.8
44442	9562	3.81(0.58)	15.0	60.5	1372.6

0420-01

This quasar is an optically violent variable (Webb *et al.* 1988) which undergoes prolonged, 2 magnitude outbursts in the optical band. The optical magnitudes were corrected for emission lines of CII at 1909 angstroms and of MgII at 2798 angstroms, both lines were redshifted by z = 0.915. The x-ray observation was made the same day as the optical measurement and came five months after a major optical flare.

The short x-ray observation, 514 sec, registered only 31.3 +/- 6.2 counts over 8 channels. Poor counting statistics prevented a significant spectral fit, so the canonical spectral index of 0.7 was used to compute the flux. The monochromatic flux density at 2 KeV for this observation is 1.41(.28) x 10^{-30} ergs/cm^2-sec Hz.

3C 120

The extremely variable Seyfert galaxy 3C 120 was observed by EINSTEIN five times during 1979 and 1980. The optical observations were made using short exposure times and fixed iris methods to minimize the effects of the galaxian component on the continuum flux (Webb *et* al., 1988) During the 1979 x-ray observations, 3C 120 was near an optical minimum A small optical outburst (about 0 8 magnitude) occurred in early 1980, and it was still bright for the 8/18/80 x ray observation

Of the five x-ray observations, two were made with the HRI detector The HRI observations are hereafter denoted by a capital H after the sequence number Independent spectral fits of the three IPC observations yielded similar spectral indices, 1 63(0 1) for #350, 1 38(0 25) for #351, and 1 50(0 46) for #1939 Since the uncertainty in establishing the spectral index was larger than the variation in the values obtained, we chose to use the best observation, #351, to determine the spectral index All observations, including the HRI observations, were reduced using the value of 1 38 for the spectral index The fitted column density was extremely close to the galactic value, so no intrinsic absorption was necessary The last two observations are HRI observations with a systematic error of 6% similar to the IPC errors The fluxes are nearly constant

TABLE 4
3C 120 X-RAY OBSERVATIONS

J D (-2 400,000)	SEQ #	FLUX DENSITY $(x10^{-29})$	DT (DAYS)	COUNTS	LIVE TIME
44100	1939	1 30(0 09)	34 0	537 7	831 1
44105	351	1 30(0 08)	30 0	18474 9	30293 9
43941	350	2 02(0 12)	20 0	15360 7	14178 1
44122	4908H	1 16(0 07)	14 0	623 0	4153 3
44469	6389H	1 01(0 07)	18 0	986 0	8844 8

except for observation 350, where the variation is a 7σ effect This observation has a very high count rate so it is unlikely that this deviation is merely statistical

NRAO 190

NRAO 190 is another OVV quasar, which has been monitored at RHO since 1969. It has shown a total variability range of over four magnitudes and rapid fluctuations in excess of 2 magnitudes. Two strong emission lines with redshifts of 0.85 are present in the spectrum of this source. The CIII line at 1909 angstroms and the Mg line at 2798 angstroms were subtracted from the optical flux. The optical spectral index is 1.00. The optical reddening determined from the Burstein and Heiles maps was 0.03

Unfortunately the x-ray observation of 6/6/80 was made three months after the nearest optical observation of 3/6/80. This x-ray observation was not of sufficient quality to determine the spectral index, so the canonical value was assumed. The resulting x ray flux was 5.34(1.05) x 10^{-31} ergs/cm^2-sec-Hz

0735+17

PKS 0735+17 is a well known Blazar that has shown optical variations exceeding three magnitudes (Webb *et al.*, 1988). Urry (1984) gave a redshift of 0.424 for this BL Lacertae source

Of the five x-ray observations made with the EINSTEIN IPC, two were made on the same night that optical exposures were made at RHO. Only one x ray observation, sequence number 5695, had a sufficient number of counts to reliably determine the spectral parameters. The fitted spectral index, 2.5(0.3), was also used to reduce the other observations. The fitted column density was larger than the galactic value, indicating intrinsic absorption for this source. The results of the x-ray observations for 0735+17 are listed in Table 5.

TABLE 5.
PKS 0735+17 X-RAY OBSERVATIONS

J.D. (-2,400,000)	SEQ #	FLUX DENSITY ($\times 10^{-30}$)	DT (DAYS)	COUNTS	LIVE TIME
43971	1991	1.77(0.21)	9.0	130.8	2112.2
44165	1992	1.26(0.18)	20.0	82.6	1582.8
44329	5695	1.38(0.07)	12.0	1832.3	34761.9
44521	7496	1.36(0.13)	0.0	242.1	3702.4
44689	7497	1.69(0.35)	0.0	61.0	3694.2

OI 363

The quasar OI 363 is one of the Ohio radio sources monitored optically at RHO. The optical observation, made about a month after the x-ray observation, was corrected for an emission line of MG II at 2798 angstroms and galactic reddening E(B-V) of 0.03. The magnesium line has a redshift of z = 0.63.

The x-ray observation registered only 8.4 counts per channel, so little spectral information was available. The canonical x-ray spectrum was used to compute an x-ray flux density of 6.7(1.0) x 10^{-31} ergs/cm^2-sec-Hz.

OI 090.4

Another Ohio radio source, this BL Lacertae object has no measured redshift. The optical variations show a range of 2 magnitudes. The source was optically bright when the x-ray observation was made in

April of 1979, six days after the optical observation. The reddening due to galactic dust in the direction of OI 090.4 was negligible.

Since the x-ray observation was of insufficient quality to determine the spectral parameters, the canonical spectrum was used to compute a flux density of 8.9(1.3) x 10^{-31} ergs/cm^2-sec-Hz.

0846+51

The optical flux of this BL Lac was corrected for weak carbon lines at 1549 and 1909 angstroms. The optical spectral index is 1.61 and Burstein and Heiles gave a reddening value of 0.0 in the direction of this source.

The x-ray observation was reduced using the canonical spectral parameters because of the low count rate in the IPC detector. A monochromatic flux of 1.14(5.0) x 10^{-31} ergs/cm^2-sec-Hz was calculated from the x-ray observation. The time between the x-ray and optical observations was 47 days.

OJ 287

This popular and well studied BL Lacertae source has a redshift of 0.306 and an optical spectral index of 0.98. Optical monitoring studies show that this source is variable over a five magnitude range, although little activity was observed between 1979 and 1981.

While both x-ray observations yielded a spectral index of 2.5 and similar hydrogen column densities, the flux differed by a factor of 5.3. This variation is roughly an 8σ effect. Table 6 shows the dates and results of the x-ray observations of OJ 287.

TABLE 6.
OJ 287 X-RAY OBSERVATIONS

J D (2 000,000)	SEQ#	FLUX DENSITY ($\times 10^{-30}$)	DT (DAYS)	COUNTS	LIVE TIME
44172.5	1993	5.78(0.35)	150.0	8063.9	20183.8
44343.5	1994	1.10(0.07)	2.0	183.2	2300.6

The second x-ray observation, 1994, was made just two days before the source was observed from RHO. Unfortunately, the nearest optical measurement to the first x-ray measurement, 1993, was several months later.

0906+01

PKS 0906+01 is a quasar with an emission line redshift of 1.018. The strong Mg II line at 2798 angstroms and the weak line of C III were subtracted from the observed brightness to obtain the continuum brightness. An optical spectral index of 0.70 was used to convert B magnitudes to monochromatic flux at 2500 angstroms in the rest frame of 0906+01.

The x-ray observation was made only seven days before the optical observation of 5/27/79. The x-ray observation yielded a low count rate, so the canonical spectrum was assumed to calculate the x-ray flux. The total 2 KeV monochromatic flux density was 5.81(1.2) x 10^{-31} ergs/cm^2-sec-Hz.

MRK 421

Markarian 421 is an elliptical galaxy with an emission line redshift of 0.031. Optical exposures were limited to 2 minutes to reduce the contamination of the nuclear continuum by the galactic component. Fixed iris tests showed that limiting the exposure time was sufficient to restrict the nebulous contribution to values less than the normal photographic errors.

The optical and x-ray observations were made only three days apart. The power law fit yielded a spectral index of 1.25 and the hydrogen column density was consistent with no intrinsic or intervening gas. A 2 KeV flux density of $3.45(0.2) \times 10^{-29}$ ergs/cm^2-sec-Hz was determined from the x-ray observation.

3C 273

First thought to be the prototype of all quasars, 3C 273 turned out to be an atypical, high luminosity quasar. Optical variability studies showed that this quasar varies over a one magnitude range while exhibiting outbursts of several tenths of a magnitude on timescales of weeks. Several strong lines were removed from the optical observations and an optical spectral index of 0.0 was used.

Four x-ray observations were analyzed for this source, of which two were made within three days of RHO optical observations. An x-ray spectral index of 0.5 fit all three IPC observations extremely well. The best fit column densities also agreed well within errors. Table 7 lists the fluxes and errors calculated for each observation. Observation 569H was originally reduced at SAO but subsequent analysis showed the BAL value was incorrect. The observation was reprocessed by Dr. Daniel Harris of SAO at the author's request, but the count rate was not available at the time of writing.

TABLE 7.
3C 273 X-RAY OBSERVATIONS

J.D. (-2,400,000)	SEQ #	FLUX DENSITY ($x10^{-29}$)	DT (DAYS)	COUNTS	LIVE TIME
43855	569H	8.38(0.51)	3.0	----	96041.4
44044	2037	5.51(0.34)	0.0	5165.0	1740.4
44239	5692	4.78(0.29)	23.0	9415.4	3910.7
44506	9310	8.63(0.53)	21.0	7448.6	1668.1

1308+32

Only one x-ray observation of this BL Lacertae source was available. A redshift of 0.996 was listed by Hewitt and Burbidge (1986) for this optically active source. A 2.5 magnitude optical outburst occurred in mid-1980 close to the epoch when the x-ray observation was made. The closest RHO optical measurement to the 6/30/80 x-ray measurement was made on 7/4/80, a delay of five days.

The 3444.3 second x-ray observation was off axis by 18.2 arc minutes. Only 336.1 counts were recorded, so a reliable chi-square spectral fit was impossible. As a result of the low count rate, we used the canonical spectrum to compute a flux density of 1.82(0.15) x 10^{-30} ergs/cm^2-sec-Hz. It is unfortunate that the x-ray observers were not aware of the dramatic optical activity of 1308+32. Several x-ray observations at this optically active epoch could have provided important data for determining the relationship between the x-ray and optical emitting regions.

OQ 172

We reduced two x-ray observations of this high redshift (Z=3.53) quasar, both observations were made within four days of the optical observation of 7/26/79. Neither x-ray observation was of sufficient quality to determine the spectral parameters. The x-ray results are given in Table 8.

TABLE 8.
OQ 172 X-RAY OBSERVATIONS

J. D. (-2,400,000)	SEQ #	FLUX DENSITY ($\times 10^{-31}$)	DT (DAYS)	COUNTS	LIVE TIME
44076	2050	3.80(0.69)	4.0	52.8	2786.6
44083	2051	2.39(0.49)	3.0	61.4	3334.9

1510-08

PKS 1510-08 is a low redshift (z = 0.34) quasar that has been actively monitored at RHO since 1969. Although the source shows a variability range of nearly two magnitudes, there was little optical activity in 1980 when the x-ray observation was made.

The source was observed by EINSTEIN eight days before the 2/18/80 optical observation. The x-ray exposure was 1400 seconds long and registered only 192(15.0) counts. Because this low count rate prevented a spectral fit, the flux density was calculated from the canonical spectral index as $2.48(0.24) \times 10^{-30}$ ergs/cm^2 sec Hz.

AP LIBRAE

AP Librae is an optically active BL Lacertae object, but has a measured redshift of z = 0.049. This object lies in a highly reddened direction and an E(B-V) of 0.12 was used to correct the optical magnitudes

The four x-ray observations were reduced using the canonical spectrum because none of the x-ray observations were of sufficient quality to determine the spectral parameters with any confidence. Table 9 gives the results of the four x-ray observations.

TABLE 9.
AP LIBRAE X-RAY OBSERVATIONS

J D (-2,400,000)	SEQ #	FLUX DENSITY ($\times 10^{-30}$)	DT (DAYS)	COUNTS	LIVE TIME
43930	1997	2.21(0.20)	30.0	143.3	1742.2
44088	1998	0.10(0.01)	8.0	222.9	1966.2
44645	7493	1.48(0.19)	1.0	108.3	2352.4
44643	9647	1.75(0.20)	4.0	156.4	2569.2

The x-ray observations show an ten sigma variation between observations 1997 and 1998.

1538+14

A Lacertid with no emission lines, 1538+14 was observed with EINSTEIN six days after it was observed at MHO. Essentially no optical extinction is seen in the direction of this source.

The low x-ray count rate prevented the chi-square fitting procedure from determining the x-ray spectral parameters but the canonical spectrum gave a flux density of 7.55(0.79) x 10^{-31} ergs/sec-cm^2 Hz

3C 345

This strong radio quasar has been a heavily observed standard at RHO since 1971. Unfortunately, no optical observations were made within 12 days of any x-ray observation. Two of the x-ray observations were made at dates more than 2 months away from any RHO optical observation. This is surprising given the frequency this source is observed at RHO. A reddening of E(B-V) = 0.03 and an emission line of MG II at 2798 angstroms was used to correct the optical magnitudes. A redshift of z = 0.595 is deduced from the emission line.

The x-ray observations are listed in Table 10. The observations show no x-ray variability at the 3 sigma level, although the optical brightness changed by 0.6 magnitude between x-ray observations 2060 and 2061.

TABLE 10.
3C 345 X-RAY OBSERVATIONS

J D (-2,400,000)	SEQ #	FLUX DENSITY $(\times 10^{-30})$	DT (DAYS)	COUNTS	LIVE TIME
44112	2060	2.75(0.23)	12.0	331.5	1959.9
44262	2061	2.99(0.24)	78.0	406.7	2037.8
44281	5694	3.36(0.24)	60.0	720.1	3280.4
44469	9261H	3.38(0.23)	17.0	66.0	2205.0

The flux was calculated using the best fit x-ray spectral index of $\alpha_x = 0.40$ obtained from observation 5694. Because this was the highest quality x-ray observation, this α_x value was used to reduce the other x-ray observations. The best fit hydrogen column density was consistent with no absorption outside of our galaxy.

3C 351

This frequently observed radio-loud quasar lies in a direction of relatively little galactic obscuration, with E(B-V) = 0.0. The optical spectrum exhibits three prominent emission lines with a redshift of 0.371. The lines at 2798, 4861 and 5007 angstroms (rest wavelengths) were subtracted from the optical magnitudes to obtain the continuum magnitude.

This quasar was observed eight times with the EINSTEIN x-ray telescope, and all eight of those observations were reduced for this research. Table 11 lists the x-ray results based on an x-ray spectral index of 0.28 derived from the power-law fit to observation 5688.

TABLE 11.
3C 351 X-RAY OBSERVATIONS

J D (-2 400 000)	SEQ #	FLUX DENSITY ($x10^{-31}$)	DT (DAYS)	COUNTS	LIVE TIME
43878	510	8.43(1.46)	73.0	75.6	1791.5
43971	2062	6.79(1.02)	6.0	86.3	2764.0
44040	2063	3.78(0.80)	8.0	44.7	1820.0
44073	4207H	13.77(2.00)	3.0	41.0	3938.2
44079	4208	3.45(0.71)	3.0	59.7	3229.2
44329	5688	6.78(0.48)	11.0	1356.7	39539.9
44573	5716	6.28(0.98)	70.0	70.9	4112.3
44593	9378	7.33(1.53)	70.0	67.8	3446.3

The HRI observation (4207) was much brighter than any of the IPC observations by a factor of 1.63. The discrepancy between this observation and the IPC observations implies we should be cautious of variations based on the HRI flux. As was mentioned in an earlier section on the HRI uncertainties, the errors involved in estimating HRI fluxes are not as well studied as the IPC errors. The possibility of a gain problem in the HRI could cause the artificially high flux measurement. Close examination of the HRI computer printout associated with the data reduction failed to reveal an obvious error so we have included this point in the analysis.

1727+50

PKS 1727+50 is a Lacertid with a redshift of 0.055. Optical observations were made within two days of both x-ray observations. No strong emission lines are present in the optical spectrum, and essentially no reddening was indicated from galaxy count and column density measurements. The x-ray observations are given in Table 12. The spectral parameters were determined from observation 2004.

TABLE 12.
1727+50 X-RAY OBSERVATIONS

J.D. (-2,400,000)	SEQ #	FLUX DENSITY (x10^{-29})	DT (DAYS)	COUNTS	LIVE TIME
44079	2004	1.24(0.08)	2.0	1495.0	2547.5
44461	9389	0.95(0.07)	1.0	818.0	1937.1

The x-ray observations indicate variability at the three-sigma level. Two optical observations contemporaneous with x-ray observations showed a 0.4 magnitude variation. The variability implied by these observations is examined more closely in the next section.

1749+09

This quasar was observed at RHO the same night EINSTEIN was observing it. A significant amount of reddening, $E(B-V) = 0.15$, was used to compute the optical flux. The low count x-ray observation was reduced using the canonical x-ray spectrum, and the resulting flux was 5.58(1.4) x 10^{-31} ergs/cm^2-sec-Hz.

1749+70

PKS 1749+70 is a Lacertid which was observed simultaneously at RHO and with the IPC aboard **EINSTEIN**. No redshift or emission lines were found in the literature for this source. A small amount of reddening, E(B-V) = 0.03, was used to compute the continuum flux. As with the previous source, the canonical spectral parameters were used to determine a flux of F = 7.93(1.2) x 10^{-31} ergs/cm^2-sec-Hz.

3C 371

This strong radio source exhibits a Lacertid type optical continuum but seems to be embedded in an elliptical galaxy. A redshift of 0.052 is given by Hewitt and Burbidge (1986) and a small amount of reddening was seen by Burstein and Heiles (1982). This is another source that was observed simultaneously in the optical and x-ray bands. A flux of 2.13(0.29) x 10^{-30} ergs/cm^2-sec-Hz was derived from 86 counts using the canonical spectral index of 0.7 and the galactic column density in the direction of the source. Again, this source was observed simultaneously at x-ray and optical frequencies.

OV-236

This quasar has a redshift of 0.353 and is a strong radio source. The optical flux was computed using an E(B-V) of 0.9 and an intrinsic reddening of E(B-V) = 0.4. The x-ray observation was of sufficient quality to determine an x-ray spectral index of 1.81. The flux was calculated using this spectral index and a fitted column density consistent with extragalactic absorption. The calculated flux density was 7.83(0.8) x 10^{-30} ergs/cm^2-sec-Hz. The x-ray observation was made on the same day as the RHO optical observation.

2128-12

PKS 2128-12 is a quasar with a redshift of z = 0.501. The optical observation was corrected for two strong emission lines, one at 2798 angstroms and the other at 4340 angstroms. There is negligible reddening in the direction of this source (Burstein and Heiles 1982).

The x-ray observation was made ten days before the RHO observation, an x-ray spectral index of 0.63 was determined from the x-ray observation. The hydrogen column density derived from the x-ray fit was consistent with the galactic column density in that direction. The resulting x-ray flux density was 2.19(0.17) x 10^{-30} ergs/cm^2-sec-Hz.

2135-14

This quasar has a redshift of 0.20 and an optical spectral index of 0.60. Three lines were subtracted from the optical magnitudes, one at 4340, one at 4861 and a line at 5007 angstroms. An E(B-V) of 0.03 was used to redden the optical magnitudes.

An extremely long x-ray exposure, 12,901 seconds, resulted in a fitted spectral index of 0.88 and a column density consistent with the galactic value. The x-ray flux density at 2 KeV was 4.75(0.30) x 10^{-30}

ergs/cm^2-sec-Hz. The time delay between the x-ray and optical observations was one day.

2155-30

PKS 2155-30 is a Lacertid with a redshift of 0.117. Three x-ray observations of this source were available and all three were reproduced for this work. Table 13 gives the results of the x-ray observations. The x-ray spectral index from observation 5201 was used to calculate the fluxes in all three observations.

TABLE 13.
PKS 2155-30 X-RAY OBSERVATIONS

J.D. (-2,400,000)	SEQ #	FLUX DENSITY ($\times 10^{-29}$)	DT (DAYS)	COUNTS	LIVE TIME
44208	3912H	7.67(0.41)	13.0	10167.6	10176.6
44182	5201	1.09(0.19)	0.0	36537.0	9054.4
44371	5202	6.21(0.38)	62.0	22765.0	6811.0

2200+42

PKS 2200+42, commonly called BL Lacertae, was the original Lacertid type AGN. It has a redshift of 0.068 but no emission lines to effect the optical continuum. This source has been observed at RBO for 17 years and has shown rapid variations over a two magnitude range. The optical and x-ray observations were made on the same night.

The x-ray observation yielded a steep spectral index of 2.25 and indicated a column density greater than the galactic value. This source showed the largest intrinsic column density of all the sources in this study. An intrinsic E(B-V) of 1.5 is found if one assumes the gas to dust ratio in the source is the same as in our galaxy. This assumption led on to unrealistic luminosity for this already luminous source, so the E(B-V)'s were scaled as discussed in the optical data reduction section. This led to an E(B-V) of 0.5 which, although still high, is believable in light of emission line studies of other high luminosity AGN. The x-ray flux was 1.66(0.15) x 10^{-29} ergs/sec-cm^2 Hz.

2201+31

The optical magnitude for this source, with a redshift of 0.297 was corrected for seven emission lines. The strongest lines were three hydrogen and two oxygen lines (Pica 1982).

The x-ray observation for this quasar was made the same night it was observed at RHO. The low count x-ray exposure was reduced with the canonical spectral index and the galactic column density appropriate for its direction. The calculated flux was 5.68(0.56) x 10^{-30}.

2216-03

This quasar, with a redshift of 0.901, was observed optically six days after the x-ray observation was made. The optical magnitude was corrected for two emission lines, C III at 1909 angstroms and MG II at 2798 angstroms. Moderate galactic reddening, E(B-V) = 0.03, was also used to correct the optical flux.

The x-ray observation was reduced using the canonical spectral parameters and yielded a flux of 7.91(1.3) x 10^{-31}.

3C 446

This source is a well-known optically violent variable which, when bright, looks like a BL Lac object. It is a high redshift object with $z = 1.404$. The optical observation was made only two days after the x-ray exposure was taken.

Since the number of total counts was small, the x-ray observation was reduced with canonical spectral parameters and the resulting flux was $2.18(0.24) \times 10^{-30}$.

2230+11

This quasar has a redshift of 1.03. No strong emission lines are present, but a small amount of galactic reddening with $E(B-V) = 0.03$ was used to compute the optical flux density. The x-ray observation was not of sufficient quality to determine the spectral parameters, so the canonical x-ray spectrum was assumed. The x-ray flux density was $1.57(0.14) \times 10^{-30}$ ergs/cm^2-sec-Hz. The time delay between the x-ray and optical observation was eight days.

2345-16

A quasar with a redshift of 0.60, this source has one strong emission line at 2798 angstroms and very little reddening, $E(B-V) = 0.01$. Again, as with the previous object, the one x-ray observation wasn't long enough to determine accurately the spectral parameters. The flux calculated by assuming the canonical x-ray spectrum is $6.87(1.33) \times 10^{-31}$ ergs/cm^2-cm-sec. The time delay between the x-ray and optical observations of this source was twenty days.

The results of the flux density calculations for all of the x-ray and optical observations analyzed here are summarized in Table 14. The sequence number is given in column 2. Column 3 and 4 list the adopted optical and x-ray spectral indices respectively. Some of the x-ray spectral indices listed in the fourth column are followed by asterisks. These asterisks signal that the observations were of low quality and no spectral information was available. The adopted x-ray spectral indices are therefore the canonical value of 0.7. The corresponding hydrogen column densities N_h are the galactic values measured in the direction of the source. The hydrogen column densities of column 5 are in units of 10^{20} atoms/cm^2. Intrinsic or intervening hydrogen absorption is indicated by an asterisk following the column density. Finally, the logs of the flux densities in units of ergs/cm^2-sec-Hz are in Columns 6 and 7. All of the observations are plotted in Figure 1. Both the x-ray flux density at 2 KeV and the optical flux density at 2500 angstroms are evaluated in the rest frame of the source. The error bars reflect the uncertainties described earlier in this chapter.

Intrinsic Column Densities

The x-ray spectral fits of nine sources indicated the hydrogen column densities were larger than the galactic value. Table 15 lists the sources which required intrinsic column densities. Column 2 lists the sequence number of the observation. Columns 3 and 4 list the galactic column density in the direction of the source and the x-ray column density determined from the x-ray spectra. The uncertainties in the fitted column densities are listed in column 5. The intrinsic

TABLE 14.
X RAY AND OPTICAL OBSERVATIONS

SOURCE	SEQUENCE NUMBER	α_o	α_x	N_H $(X10^{20})$	$LOG(F_o)$ (2500A)	$LOG(F_x)$ (2KeV)
0007+10	10125	1.75	1.50	31.62*	-25.804	-29.499
0035+12	7508	0.00	0.70*	5.23	-26.483	-30.720
3C 66A	7725	2.63	1.63	17.78*	-25.720	-29.843
0235+16	5691	3.00	1.60	70.00*	-25.952	-29.649
0235+16	7506	3.00	1.60	70.00*	-26.644	-29.763
0235+16	7507	3.00	1.60	70.00*	-25.948	-29.463
0235+16	9283	3.00	1.60	70.00*	-26.788	-29.539
0235+16	9285	3.00	1.60	70.00*	-25.952	-29.397
0235+16	9562	3.00	1.60	70.00*	-25.952	-29.419
0420-01	2016	0.70	0.70*	7.78	-26.803	-29.850
3C 120	350	1.30	1.38	10.00	-25.753	-28.694
3C 120	351	1.30	1.38	10.00	-25.801	-28.886
3C 120	1939	1.30	1.38	10.00	-25.801	-28.884
3C 120	4908H	1.30	1.38	10.00	-25.801	-28.935
3C 120	6389H	1.30	1.38	10.00	-25.593	-28.995
NRAO 190	2018	1.00	0.70*	5.73	-27.043	-30.272
0735+17	1991	0.97	1.50	10.00*	-25.865	-29.753
0735+17	1992	0.97	1.50	10.00*	-25.745	-29.899
0735+17	5695	0.97	1.50	10.00*	-25.757	-29.859
0735+17	7496	0.97	1.50	10.00*	-25.517	-29.868
0735+17	7497	0.97	1.50	10.00*	-25.661	-29.771
OI 363	3993	0.07	0.70*	4.96	-26.058	-30.174
OI 090.4	550	1.00	0.70*	2.71	-25.758	-30.048
0846+51	5228	1.61	0.70*	2.23	-27.301	-30.944
OJ 287	1993	0.98	1.50	3.16*	-25.841	-29.238
OJ 287	1994	0.98	1.50	3.16*	-25.889	-29.960
0906+01	2029	0.70	0.70*	3.10	-26.651	-30.236
MRK 421	5207	1.64	1.25	1.77	-25.290	-28.462
3C 273	569H	0.00	0.80	1.80	-24.502	-28.077
3C 273	2037	0.00	0.50	1.00	-24.590	-28.259
3C 273	5692	0.00	0.50	1.00	-24.598	-28.321
3C 273	9310	0.00	0.50	1.00	-24.558	-28.064
1308+32	5205	1.20	0.70*	1.08	-25.663	-29.741
OQ 172	2050	0.50	0.70*	1.73	-26.769	-30.420
OQ 172	2051	0.50	0.70*	1.73	-26.769	-30.620
1510-08	2053	0.90	0.70*	7.60	-26.205	-29.606
AP LIB	1997	2.51	0.70*	8.84	-25.880	-29.655
AP LIB	1998	2.51	0.70*	8.84	-25.860	-30.991
AP LIB	7493	2.51	0.70*	8.84	-25.708	-29.830
AP LIB	9647	2.51	0.70*	8.84	-25.708	-29.757
1538+14	7728	0.90	0.70*	3.15	-26.740	-30.122
3C 345	2060	1.11	0.40	1.05	-26.264	-29.560
3C 345	2061	1.11	0.40	1.05	-26.024	-29.525
3C 345	5694	1.11	0.40	1.05	-26.024	-29.473
3C 345	9261H	1.11	0.40	1.05	-26.168	-29.471
3C 351	510	0.50	0.28	2.36	-25.938	-30.074

TABLE 14- CONTINUED

SOURCE	SEQUENCE NUMBER	α_o	α_x	N_h (X10^{20})	LOG(F_o) (2500A)	LOG(F_x) (2KeV)
3C 351	2062	0.50	0.28	2.36	25.898	30.168
3C 351	2063	0.50	0.28	2.36	-25.846	-30.422
3C 351	4207H	0.50	0.28	2.36	25.846	29.861
3C 351	4208	0.50	0.28	2.36	25.906	-30.462
3C 351	5688	0.50	0.28	2.36	-25.966	-30.169
3C 351	5716	0.50	0.28	2.36	-25.934	-30.202
3C 351	9378	0.50	0.28	2.36	-25.962	-30.135
1727+50	2004	1.60	0.75	2.70	-26.355	-28.906
1727+50	9389	1.60	0.75	2.70	-26.507	-29.023
1749+09	7175	0.91	0.70*	9.79	-26.666	-30.253
1749+70	2720	1.34	0.70*	4.00	-26.270	-30.101
3C 371	1967	1.15	0.70*	4.96	-25.531	-29.671
OV 236	3890	0.70	1.81	74.99*	-25.249	-29.106
2128 12	8413	0.40	0.63	6.68*	26.140	29.660
2135 14	5426	0.60	0.88	5.48*	-25.854	-29.323
2155-30	3912H	0.64	1.06	1.73	-25.118	-28.115
2155-30	5201	0.64	1.75	1.73	-25.046	-28.962
2155-30	5202	0.64	1.75	1.73	-25.074	-28.207
2200+42	5693	1.90	2.25	100.00*	-25.098	-28.780
2201+31	7182	0.01	0.70*	88.30	-25.701	-29.246
2216-03	2068	1.24	0.70*	5.63	-26.196	-30.102
3C 446	8022	1.60	0.70*	5.28	-25.628	-29.662
2230+11	4042	0.67	0.70*	5.35	-26.609	-29.805
2345-16	2076	0.70	0.70*	1.85	-26.620	30.163

NOTES

1. An H in column 2 indicates the observation was made with the High Resolution Imager

2. An * in column 4 indicates a canonical spectrum with index 0.7 was used

3. An * in column 5 indicates the hydrogen column density of the x-ray fit was greater than the galactic value

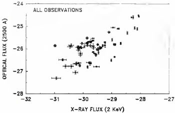

Figure 1 The xray and optical flux observations from Table 3 are plotted. The log of the x-ray flux is the abscissa and the log of the optical flux, both in units of ergs/sec cm^2 Hz. The error bars represent one sigma errors

reddening is calculated by inserting the excess column density into equation (2-3) is listed in Column 6. We find that some Lacertids and some quasars required some intrinsic column density.

TABLE 15.
EXCESS COLUMN DENSITIES

SOURCE NAME	OBS #	GALACTIC N_h (x 10^{20})	FITTED N_h (x 10^{20})	UNCERTAINTY IN FITTED N_h	E(B-V) EXCESS
0007+10	10125	5.85	31.62	(+11.81/-9.23)	0.457
3C 66A	7725	7.51	17.78	(+18.99/-15.6)	0.149
0235+164	5691	8.92	70.00	(+197.6/-37.8)	1.158
0735+17	1991	4.60	10.00	(+2.84/-0.21)	0.005
OJ 287	1993	2.93	3.16	(+1.75/-0.96)	0.000
OV-236	2890	7.50	75.00	(+44.81/-22.9)	1.280
2128-12	8413	4.73	6.67	(+3.64/-2.27)	0.000
2135-14	5426	4.59	5.48	(+1.62/-0.31)	0.000
2200+42	5683	19.10	100.00	(+116.9/-48.4)	1.552

The reddening is calculated by inserting the excess column density into equation (2-3). Elvis et al. (1986) examined eight PG quasars with high count IPC observations and found intrinsic column densities consistent with but not required by their observations.

X-Ray Variability

Eleven sources have multiple x-ray observations which can be used to investigate x-ray variability. Tananbaum et al. (1979) found evidence that the quasar OX 169 varied significantly in the x-ray band on timescales of several hours. Worrell et al. (1979) found that 3C 273 also exhibited significant x-ray variability but on timescales of months. McHardy (1985) concluded that radio-loud quasars are more likely to be variable in x-rays than are radio-quiet quasars. Long term variability (months to years) was seen in about half of the 28 quasars studied by Marshall _et al._ (1981) with EXOSAT. Medium term (days) variability was seen in a few Seyferts and quasars, but very little timing information is available for these timescales. There are indications that rapid variability (seconds) is also present, but again more sophisticated detectors and more observations are needed.

The data presented in Tables 3 through 13 can be used to investigate the realities of x-ray variability in these 11 sources. We define a source as being variable in x-rays if two conditions are met. The first condition is that the extreme flux measurements must differ by at least 3σ. We determine this by simply subtracting the faintest flux from the brightest, and dividing by their errors added in quadrature. The second condition is that the variations exhibited by the data must give a chi-square probability that the source is variable of over 95%. Table 16 gives the results of the variability analysis. The first two columns list the source name and the total number of x-ray observations available for that source.

TABLE 16.
X-RAY VARIABILITY

SOURCE	OBS. #	δF_{max}	σ	P	var
0235+164	6	2.28×10^{-30}	5.6	>99.5	Y
3C 120	5	0.72×10^{-29}	4.9	>99.5	Y
0735+17	5	0.51×10^{-30}	2.6	70.0	N
OJ 287	2	4.68×10^{-30}	13.1	>99.5	Y
3C 273	4	3.85×10^{-29}	6.3	>99.5	Y
OQ 172	2	1.41×10^{-31}	1.7	99.0	N
AP LIB	4	1.66×10^{-30}	10.5	>99.5	Y
3C 345	4	0.63×10^{-30}	1.9	90.0	N
3C 351	8	9.99×10^{-31}	4.6	>99.5	Y
1727+50	2	0.29×10^{-29}	2.7	>99.5	N
2155-30	3	6.58×10^{-29}	14.6	>99.5	Y

In the third column is the difference between the brightest and faintest flux measurements. Column 4 is the significance of the variation in σ's and column 5 gives the chi square probability, P, that the source is indeed variable. The last column, column 6, indicates whether the source satisfies both criteria for variability, a Y meaning yes and an N signifying that it doesn't. Seven out of the eleven sources show x-ray variability according to our definition. The x-ray flux curves are shown in Figures 2 through 12 along with all of the Rosemary Hill data around the x-ray observation dates. These plots illustrate the relative activity in both bands. In each figure, the top graph shows the x-ray flux at 2 Kev in units of millijanskys and the lower panel shows the optical light curve, also in millijanskys.

Figure 2 shows the flux curves of AO 0235+164. A series of obvious optical flares are present, representing a factor of five change in the flux level. An x-ray flare which peaked on J.D. 44455 shows a variation of a factor of five. The time delay between the x ray flare and the optical flare, which peaked on J.D. 44556, is 101 days. A similar x-ray and optical flare separated by a time delay was reported for the OVV quasar 1156+295 by Webb and McHardy (1985). In that case, a similar x ray flare was seen during a series of three optical bursts with the x-ray flare preceding the largest optical flare. The two optical maxima in Figure 2 correspond to 17^{m}17 and 17^{m}09 respectively, while the faintest point corresponds to 19^{m}9. A variability test of the optical data gave a maximum optical variation of over 12σ and a chi square probability of over 99.5%.

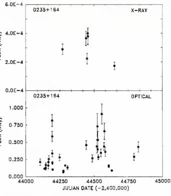

Figure 2 The x-ray and optical flux curves of AO 0235+164. The X ray observations are from Table 3 and the optical observations are all photographic observations made at Rosemary Hill observatory. The fluxes are monochromatic fluxes at 2500 angstroms and 2 Kev for the optical and x-ray fluxes respectively

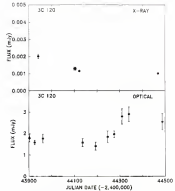

Figure 3 The x-ray and optical flux curves of 3C 120 The fluxes and units are the same as in Figure 2

The x-ray and optical flux curves of 3C 120 are shown in Figure 3. Table 15 indicates the x-ray variation is significant, and a test of the optical data indicates it is also variable. The upward trend of the optical data is not seen in the x-ray flux curve. Unfortunately the 347 day gap in the x-ray flux curve is placed where we would expect an x-ray flare.

Figure 4 shows the flux curves of PKS 0735+17. The small variation in the x-ray flux curve is not significant, as shown in Table 15. The optical flux is variable with variations up to 12σ. Again we see a general rise in optical flux level that is not reflected in the x-ray flux.

Only two x-ray points were reduced for OJ 287, but they showed significant variability. The flux curves are shown in Figure 5. The optical flux did not show significant variability during this time. The chi-square test gave a probability of >99%, but the largest variation was only 2.9σ. Unfortunately no optical observations were made near the first x-ray observation.

Observations of 3C 273 made with the HEAO 1 instrument (Bradt _et al._ 1979) showed significant x-ray variability on timescales of months. The x-ray data from Table 7 are plotted in the upper panel of Figure 6 and the RHO observations between J.D. 2 443 800 and 2 444 800 are shown in the lower panel. Both the optical and the x-ray observations exhibited significant variability. Neither the x-ray nor the optical coverage is sufficient to determine if the variations are correlated. The timescales for variations in the x-ray cannot be compared to the optical timescales because the x-ray data are separated by 150 days.

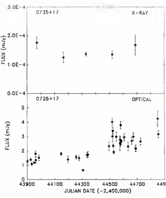

Figure 4. The x-ray and optical flux curves of 0735+17.

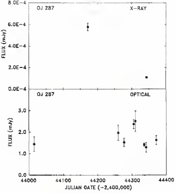

Figure 5 The x-ray and optical flux curves of OJ 287

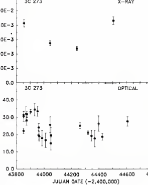

Figure 6. The x-ray and optical flux curves of 3C 273.

The x-ray flare seen in Figure 7 is not significant at the 3σ level for OQ 172. The optical variation is statistically significant, but the paucity of data prevents any real variability conclusions.

Figure 8 shows the x-ray and optical flux curves of AP Libra, and both curves are statistically variable. Without the point at J. D. 2,444,088, the x-ray variation would not be significant. Since the count rate is reasonably high, we have no evidence to doubt the reality of this variation. At the time of this "anti-flare", the optical flux varies but not dramatically. Again, insufficient optical and x-ray coverage prevents our concluding anything about correlated variability of the x-ray and optical bands.

Variability tests indicate the x-ray flux of 3C 345 in Figure 9 is constant. The optical variations during the same time interval are statistically significant by both tests. The optical flux curve seems to reflect a constantly increasing brightness level with mild fluctuations superimposed.

The flux curves of the quasar 3C 351 are shown in Figure 10. The optical flux curve is not variable by either test. The x-ray light curve shows one point much brighter than the others. This point is the HRI observation discussed earlier in the 3C 351 subsection. If we leave this point out of the variability analyses, the source is still variable, although the variation is less significant.

Figure 11 shows the x-ray and optical flux curves of 1727+50. The x-ray variation is significant by the chi-square test but represents only a 2.7σ variation. The optical variations are significant and show a maximum variation of over 4σ.

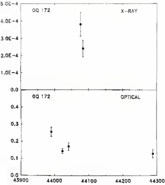

Figure 7. The x-ray and optical flux curves of OQ 172

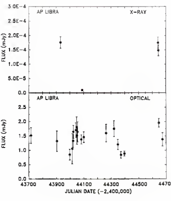

Figure 8. The x-ray and optical flux curves of AP LIBRA.

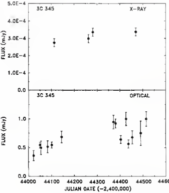

Figure 9 The x-ray and optical flux curves of 3C 345

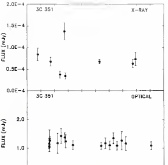

Figure 10 The x-ray and optical flux curves of 3C 351.

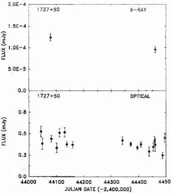

Figure 11. The x-ray and optical flux curves of 1727+50

Significant variations are seen in the x-ray flux curve (Figure 12) of 2155-30. The optical flux curve is not variable according to the statistical criteria. The chance to pick up an optical event following the dramatic x-ray "anti-flare" was lost due to the position of the quasar relative to the Sun.

Out of the six BL Lac sources, four exhibited x-ray variability while two others showed no evidence of x-ray variability. Two of the x-ray variables showed no evidence of optical variability. One of the x-ray non-variable Lacertids had only 2 data points, so the analysis is questionable. The lone Seyfert galaxy showed both optical and x-ray variability of 4.7σ or more. The x-ray variability timescale for 3C 120 was 1.4 years, while the optical timescale was 150 days. Of the four quasars, three exhibited optical variability and two showed x-ray variations. The optically non-variable source (3C 351) showed significant x-ray variability.

X-ray variation timescales ranged from 1.4 years (3C 120 at 4.9σ) to 1.0 day (4.6σ variation of 0235+164). Both rapid x-ray flares, as seen in 0235+164 and 3C 351, and long term variations such as that seen in 3C 273 are found in the data presented here. Comparison of the timescales present in the x-ray flux curves to those in optical flux curves suggests that the same physical processes could be responsible for the variations in both frequency bands.

Obviously much more timing information is needed before any solid conclusions about correlated x-ray and optical events can be found. The above analyses show that studies of this type can yield valuable

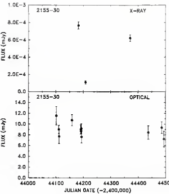

Figure 12 The x-ray and optical flux curves of 2155-30

information if the x-ray and optical observers coordinate their observations properly The time delay between x-ray and optical flares seen in 0233+164 shows that even simultaneous observations may be deceiving

CHAPTER III
CORRELATIVE ANALYSIS

Previous Results

The Einstein x-ray observations have been used extensively to examine the x-ray properties of AGN. Tananbaum et al. (1979) observed 35 previously known quasars and determined an average or "effective" x-ray optical spectral index of 1.27+/-0.07 for their sample. The x-ray optical spectral index is defined as the slope of a line connecting the point $\log(F_o)$ at 2500 angstroms to $\log(F_X)$ at 2 Kev (see equation 2-14). Kriss, Canizares and Ricker (1980) observed 37 Seyfert galaxies and found a significant correlation between the B-band continuum flux and the x-ray flux. Ku, Helfand and Lucy (1980) detected x-ray emission from 35 out of 111 quasars. They divided their sources into two classes based on radio luminosity (radio quiet $L_r < 10^{41}$ vs. radio loud $L_r < 10^{41}$). The broad-band x-ray luminosities of the first class ranged from 10^{43} to 10^{46} ergs/sec. These sources have many properties similar to Seyfert galaxies. The second class of quasars is defined as sources whose radio luminosity exceeds 10^{41} ergs/sec and includes radio-loud quasars, BL Lacertae objects and N-galaxies. Sources in this class have slightly higher x-ray luminosities, usually between 10^{44} and 10^{47} ergs/sec. The x-ray-optical slope for the radio-quiet sample was found to be 1.5, while the slope of the radio loud group was only 1.35. They also found evidence for luminosity evolution.

Tananbaum et al. (1979) and Kriss, Canizares and Ricker (1980) also studied the x-ray emission of a large number of Seyfert galaxies. They found strong correlations between the optical and the x-ray emissions, similar to those found in quasar studies.

Zamorani *et al.* (1981) reported 79 quasar detections in x-rays and found correlations between the optical and x-ray emission of these sources. Radio-loud quasars emitted three times more x-ray flux than radio-quiet quasars with the same optical luminosity. They found an average x-ray-optical spectral index of 1.4 to 1.5 in their sample.

Blumenthal, Keel and Miller (1982) found that x-ray emission is a function of optical luminosity to the 0.5 power. They also found an average x-ray-optical spectral index of 1.5, which is consistent with the Ku *et al.* results.

Schwartz and Ku (1983) detected x-ray emission from Lacertids similar to radio-loud quasars. Tananbaum *et al.* (1983) examined 33 3CR sources and found the x-ray luminosity is a function of the optical luminosity to the 0.47 power.

Avni and Tananbaum (1986) concluded that virtually all quasars are x-ray bright. Tananbaum *et al.* (1986) reported 57 detections out of 66 quasars observed. These sources were all from the Palomar bright quasar survey, which represents a nearly complete sample down to 22nd magnitude. The non-detections were presumably due to the limited sensitivity of the EINSTEIN detectors.

The effects of x-ray variability on x-ray-optical correlations are uncertain, but the excessive scatter in AGN correlations is due in part to both optical and x-ray variability. Nearly all AGN show variability, and some exhibit rapid (days) flares exceeding one to three magnitudes (Pica *et al.* 1980 and Webb *et al.* 1988). Webb (1985) concluded from a sample of 42 AGN that optical variability can have a substantial effect on x-ray-optical correlations. Variability can cause a difference in the measured L_x versus L_o exponent of 0.26. This can, in turn, alter the contribution to the x-ray background from AGN by a factor of 100. Webb also analyzed a 26-source subset of the original 42 sources whose optical fluxes could be interpolated to the x-ray observation date. This sample exhibited a stronger degree of correlation than the original sample. This result indicated that the correlations would be more meaningful if variability could be taken into account.

In this research we have attempted to acquire and reduce all x-ray observations of AGN made contemporaneous with RHO optical observations. We analyzed this sample, in addition to a number of other observations which were not precisely simultaneous. Another advantage of this data set is that the optical and x-ray observations were analyzed consistently with each other. Inspection of the x-ray and optical light curves presented in Chapter II suggests a time delay between the x-ray and optical variations. Bregman et al. (1988) detected correlated x-ray and optical variability in 3C 446 with little time delay. Since little variability data are available, we cannot correct our observations for a time delay. Even with these uncertain non-simultaneous events, we expect our data to show a significantly higher degree of correlation than previous studies.

Correlation Procedures

In correlation analyses, one hopes to establish an analytical relationship between two observable quantities. Least squares fitting procedures are commonly used to fit a model to a set of observations and determine the best values of the model parameters. In this research we utilize two different algorithms in order to determine model parameters for the data described in Chapter II.

Linear models were used because of the magnitude of the uncertainties and the scatter in the $\log(L_X)$-$\mathrm{Log}(L_D)$ plane. The use of higher order models increase the number of free parameters without increasing the significance of the fits. The initial analysis of the data was done using the multiple regression routine of Bevington (1969). The sub-program REGRES was written in FORTRAN IV and all analyses were run on a Columbia IBM clone PC using a WATFOR compiler. The algorithm fits polynomial models with linear coefficients to the data. A complete description of the algorithm used in REGRES is given in Bevington (1969). The fitting procedure allowed weighting of the dependent variable using instrumental, statistical or constant weighting. The program was used exclusively in the instrumental weighting mode, which weighted each observation with the inverse of its error squared.

The program returns the parameters a and b in equation (3-1) for a linear model.

$$Y = a + b\,X \tag{3-1}$$

in equation (3-1) X represents the independent variable and Y is the dependent variable. To calculate the correlation coefficient, we re-evaluate the solution to equation (3-1) with the independent and dependent variables interchanged. The new parameters are a′ and b′. The linear correlation coefficient is then defined as:

$$r = b \times b' \qquad (3\text{-}2)$$

The linear correlation coefficient takes on values between +1 and -1. A value of +1 indicates complete correlation while -1 indicates inverse correlation. If r is equal to 0, then no correlation is present.

The correlation coefficient r should not be used by itself to compare the degree of correlation between two sets of observations with different degrees of freedom. To compare the degree of correlation in samples with different degrees of freedom, the correlation probabilities should be compared. The correlation probability is found by constructing a parent population of completely uncorrelated data with the same number of degrees of freedom as the original sample. The probability that a correlation coefficient as large or larger than the original correlation coefficient could arise in the completely uncorrelated sample is then calculated. Bevington (1969) describes the details of this procedure and the subroutine PCORRE calculates the probability that an uncorrelated sample would exhibit a correlation coefficient as high or higher than the one obtained from the original data. This probability, properly called the integrated probability of r, is the best estimate of the degree of correlation found in the data.

independent of the number of points in the sample. We will quote both the correlation coefficient and the correlation probability for each model fit so comparison of the samples with different degrees of freedom can be made.

A second least squares method was used to refine the parameters a and b. This more sophisticated method accounts for errors in both the independent and dependent variables. This method, developed by Jefferys (1980), is a non-linear method which is independent of the form of the equations of condition. The data may appear non-linearly in the equations of condition and the parameters of the model can be correlated. The Jefferys method is essentially a generalization of the classical least squares method. The equations of condition are of the form:

$$\mathbf{f}(\mathbf{x} + \mathbf{v},\ \mathbf{a}) = \mathbf{0}, \tag{3-3}$$

where **f** is a vector function of the observations **x** and the parameters **a**. The vector **v** is the residual vector. In this section, all boldface variables are vector quantities. In this case, both the x-ray and optical fluxes are contained in **x** such that

$$\mathrm{Log}(F_X)_i = x_{2i+1}, \tag{3-4}$$

$$\mathrm{Log}(F_o)_i = x_{2i},\quad i = 1,\ldots,N. \tag{3-5}$$

Constraints on the parameters are given by the vector equation

$$\mathbf{g}(\mathbf{a}) = \mathbf{0}, \tag{3-6}$$

where the parameters **a** are the coefficients in the linear equation

$$\mathrm{Log}(F_o)_i - a_1 - a_2 \times \mathrm{Log}(F_x)_i = 0 \qquad (3\text{-}7)$$

In classical least squares, estimates of the residuals $\mathbf{v}$ and the parameters $\mathbf{a}$ are found by solving equations (3-3) and (3-6) while simultaneously minimizing the residual equation

$$S_o = \tfrac{1}{2}\mathbf{v}^t\sigma^{-1}\mathbf{v}, \qquad (3\text{-}8)$$

where $\mathbf{v}^t$ is the transpose of $\mathbf{v}$ and σ is the covariance matrix. The solution is best accomplished by using Lagrange multipliers. The Lagrange vectors Γ and μ are used to combine the condition equations, the parameter constraints, and the residual equation to form the function to be minimized

$$S = \tfrac{1}{2}\mathbf{v}^t\sigma^{-1}\mathbf{v} + \mathbf{f}^t(\mathbf{x}',\mathbf{a})\mu + \mathbf{g}^t(\mathbf{a})\Gamma, \qquad (3\text{-}9)$$

where $\mathbf{x}'$ is defined as $\mathbf{x} + \mathbf{v}$. This quantity is minimized by taking the partial derivatives of (3-9) with respect to the observations $\mathbf{x}'$, the parameters $\mathbf{a}$, and the multipliers and setting each resulting equation equal to zero. The normal equations, with partial derivatives with respect to a variable denoted by subscripts, are given by

$$\sigma^{-1}\mathbf{v}' + \mathbf{f}_x^{\,t}(\mathbf{x}',\mathbf{a})\mu = 0, \qquad (3\text{-}10)$$

$$\mathbf{f}_a^{\,t}(\mathbf{x}',\mathbf{a})\mu + \mathbf{g}_a^{\,t}(\mathbf{a})\Gamma = 0 \qquad (3\text{-}11)$$

$$\mathbf{f}(\mathbf{x}',\mathbf{a}) = 0 \qquad (3\text{-}12)$$

$$\mathbf{g}(\mathbf{a}) = 0 \qquad (3\text{-}13)$$

Following Newton's method, corrections (α,β) are added to the approximate solution $(\mathbf{x}^o,\mathbf{a}^o)$, and the normal equations are restated as

$$\sigma^{-1}(v'' + \alpha) + f_x{}^t\mu = 0 \tag{3-14}$$

$$f_a{}^t\mu + g_a{}^t\Gamma = 0 \tag{3-15}$$

$$f + f_x\alpha + f_a\beta = 0, \tag{3-16}$$

$$g + g_a\beta = 0 \tag{3-17}$$

The double primes are left off the subscripted variables in the interest of clarity. Combining equations (3-14) through (3-17) and defining the weight matrix as

$$W = (f_x\sigma f_x{}^t)^{-1} \tag{3-18}$$

the resulting reduced normal equations are

$$\begin{bmatrix} f_a{}^t W f_a & g_a{}^t \\ g_a & 0 \end{bmatrix} \begin{bmatrix} \beta \\ \Gamma \end{bmatrix} = - \begin{bmatrix} f_a{}^t W\Phi \\ g \end{bmatrix} \tag{3-19}$$

where $\Phi = f - f_x v$. The solution is used to compute new residuals from

$$v_{new} = -\sigma f_x{}^t W(\Phi + f_a\beta) \tag{3-20}$$

The new residuals are used to adjust the observations and compute new parameter values. The procedure is repeated until the residuals are less than a specified tolerance.

The algorithm was coded in FORTRAN IV by William Cooke (1987) for a parabolic equation of condition. Cooke's computer code was rewritten to fit a linear model instead of a parabolic one to the data presented in Chapter II.

The Jefferys method is an iterative procedure which requires starting values for each of the parameters. Parameter values determined in the Bevington fits were used as starting values for the Jefferys fits. The iteration process was repeated until the residuals were smaller than 0.0001. The principal advantage of this routine is that both the independent and dependent variables can have errors.

The Jefferys routine has an additional advantage. The slope of the fit using the optical flux as the independent variable is the exact inverse of the slope calculated assuming the x-ray flux is the independent variable. Least squares fits which allow error in only one variable are not invertible. One must either specify which variable was the independent one, or rerun the fitting procedure reversing the roles of the variables. This inevitably leads to non invertible values for the slopes.

Simulations by Chanan (1983) indicate the x-ray flux is the primary radiation and should be used as the independent variable. In other words, the x-ray flux determines the optical flux and should treated as the independent variable in discussing correlations. We quote most of the results using the x-ray flux as the independent variable, although the Bevington correlations were done with the x-ray flux as both the independent and the dependent variables.

Correlation Sample

The x-ray and optical data summarized in Table 14 form an excellent sample for correlation. The sample is not complete in the sense of containing all members down to a certain flux limit, but it is a varied sample of AGN in which the x-ray and optical data are nearly contemporaneous and have been reduced consistently.

Thirty-six sources are represented by the 70 observations listed in Table 14. Eleven of the sources are represented by more than one x-ray-optical pair. Since there is no basis to select a particular set of observations of any one source, all pairs were included in the correlation analyses.

The observations were divided into subsamples whose members share common characteristics. These subsamples are useful in investigating the x-ray-optical properties of certain types of objects. The objects were first sorted by optical properties, either spectral differences or optical variability characteristics. The sources were then grouped according to the time delay between the x-ray and optical observations. The following subsections contain a brief description of each of these subsamples.

OVV Subsample

The OVV subsample contains twenty observations of six optically violent variable objects. The five OVV quasars, 0420-01, NRAO 190, 3C 345, 3C 351 and 3C 446, are grouped with the OVV Seyfert galaxy 3C 120. Monitoring at RHO showed all of these sources to be OVV's. No Lacertids are included in this sample, although some Lacertids exhibit OVV variability.

BLAZAR Subsample

Twelve Lacertids and five OVV quasars make up the Blazar sample. These sources include: 3C 66A, 0235+16, 0420-01, NRAO 190, 0735+17, 0846+51, OJ 287, 1308+32, AP LIBRA, 3C 345, 3C 351, 3C 371, 1727+50 3C 371, 2155-30, 2200+42 and 3C 446.

NON-OVV Subsample

The NON-OVV subsample contains 12 quasars, the Seyfert galaxy 0007+10 and the elliptical galaxy MRK 421. None of these objects exhibit optically violent behavior, although they are all optically variable.

LACERTID Subsample

The criterion for this sample is based on spectroscopic appearance. The eleven Lacertids in Table 14 are grouped together in this subsample, which contains 27 observations of these sources.

QUASAR Subsample

Thirty-one observations of all 17 quasars are grouped together in this sample. Both OVV and non-OVV quasars are included. This sample is also a spectroscopic division, based primarily on the presence of broad emission lines in their spectrum.

QUASAR+LACERTID Subsample

The 11 Lacertids and 17 quasars are included in this sample. Only the Seyfert and elliptical galaxy observations were omitted from the total of 55 observations.

TD0 Subsample

This sample contains observations whose X-ray and optical observations were made simultaneously, i.e. 0 days time delay (hence TD0). Only eleven observations of ten sources, 6 Lacertids and 4 quasars, are included in the sample. The redshifts of these sources ranged from 0.05 to 1.74.

TDWK Subsample

All x-ray and optical observations which were made within one week are included in this sample (time delay of 1 week). A total of 29 observations are included and the average time delay is only 2 days. Nine Lacertids, 10 quasars and the elliptical galaxy MRK 421 comprise this sample.

TD2WK Subsample

All observations in this group were made within 2 weeks of each other. The average time delay is 4.8 days for these observations, which of course contains the TDWK subset. Fourteen quasars, 10 Lacertids, the 2 Seyfert galaxies and MRK 421 are included in this group. A total of 43 observations from Table 14 were contemporaneous within a 2 week period.

Flux Correlation Results

The results of correlations with all of the flux data in Table 14 are shown in Table 17. Best fit lines are plotted with the original data in Figure 13. Throughout the correlation calculations, the x-ray

Figure 13. The correlation diagram for all of the observations listed in Table 14 are shown with one sigma error bars. The best fit line determined by the Bevington routine is represented by the dashed line. The best fit line from the Jefferys routine is represented by the dotted line. The differences occur primarily because the Jefferys routine accounts for errors in both the x-ray and the optical observations.

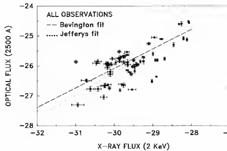
ALL OBSERVATIONS
-- Bevington fit
..... Jefferys fit
OPTICAL FLUX (2500 A)
X-RAY FLUX (2 KeV)
−24
−25
−26
−27
−28
−32
−31
−30
−29
−28
−27

flux errors are symmetricized in log space. The non-symmetric error bars arise in the transformation from flux to log flux, and the average amount of asymmetry is 17% of the total uncertainty. These asymmetries have been ignored in the correlations. The first column in Table 17 indicates whether the independent variable is the optical or x-ray fluxes. The second column indicates which correlation routine was used, and columns 4 and 5 give the slope and the correlation coefficient for each fit. The final column indicates the probability that a completely uncorrelated sample with an equivalent number of degrees of freedom would exhibit a correlation coefficient as high or higher than the one listed in column 4 (referred to earlier as the correlation probability). The correlation coefficients in Table 17 indicate a high degree of correlation between the x-ray and optical fluxes. The number of degrees of freedom is 68 in Table 17.

TABLE 17

FLUX CORRELATIONS FOR ALL 70 OBSERVATIONS

INDEPENDENT VARIABLE	CORRELATION ROUTINE	b	r	PROBABILITY OF NO CORRELATION
OPTICAL	BEVINGTON	0.75(0.01)	0.759	2.0×10^{-10}
X RAY	BEVINGTON	0.65(0.01)	0.738	4.6×10^{-8}
X-RAY	JEFFERYS	0.75(0.01)	-----	----------

It is evident that efforts to obtain contemporaneous data and reduce it consistently have increased the significance of the correlations. The slope of 0.75 from the Jefferys routine is quoted with the x ray flux as the independent variable.

The correlation results for each of the subsamples are listed in Table 18. Column 1 identifies the subsample while the second column in Table 18 lists the number of observation pairs. The third, fourth, and fifth columns contain the slope of the linear Jefferys fit, the correlation coefficient, and the probability that an uncorrelated set of data with the same number of degrees of freedom would exhibit a correlation coefficient as high or higher than the one listed in column 4. The quantities in parentheses are the standard errors of the slope.

TABLE 18.
FLUX CORRELATIONS

DATA SET	N	b	r	PROBABILITY OF NO CORRELATION
ALL	70	0.75(0.01)	0.74	4.55×10^{-8}
TDO	13	1.14(0.04)	0.79	1.20×10^{-3}
TDWK	33	0.83(0.02)	0.71	3.47×10^{-6}
TD2WK	48	0.73(0.02)	0.67	2.00×10^{-7}
LACERTID	29	0.59(0.06)	0.47	1.00×10^{-2}
QUASARS	34	0.93(0.01)	0.90	4.70×10^{-9}
QUASAR+LACERTID	63	0.81(0.01)	0.76	3.70×10^{-8}
BLAZAR	44	0.58(0.02)	0.44	2.80×10^{-3}
OVV	20	0.30(0.03)	0.32	1.70×10^{-1}
NON-OVV	19	0.99(0.01)	0.97	4.03×10^{-8}

As can be seen by inspection of Table 18, the slope for the simultaneous fit is much steeper than for all 70 observations (Table 17). The correlation coefficient is higher but due to the lower number of degrees of freedom is not as significant. As we increase the number of sources by increasing the allowable time delay, the slope approaches 0.75 and the correlation becomes more significant. The Lacertids show very little correlation and a very flat slope. When all of the quasars are analyzed together, an extremely significant correlation coefficient of 0.9 was found. The quasars exhibit a much higher slope than the Lacertids and also are more highly correlated. Correlation of the quasars and the Lacertids together shows a less significant but still correlated sample with a best fit slope of 0.81. The blazar sample shows excessive scatter and the correlation coefficient is only slightly less significant than in the simultaneous data. The slope is also much flatter. It appears that the x-ray and optical fluxes of blazars tend be less correlated than optically quiet quasars. The OVV quasars by themselves have a flatter slope and are not highly correlated. The non-OVV quasars, however, exhibit an extremely high correlation coefficient. The probability that this correlation coefficient could arise by chance is only 4.03×10^{-8} and the correlation coefficient is the largest of any of the subsamples.

We can immediately conclude that the simultaneous data are correlated but the correlation is not extremely significant. The blazar and OVV data are only slightly correlated. The non-OVV sample on the other hand, is highly correlated and the linear fit has a slope of 0.99(0.01). Figures 14 through 22 show the data and the Jefferys fits for these subsamples. Note the small amount of scatter in Figure 22.

The flux data show evidence that there is an intrinsic difference between x-ray and optical emission of non-OVV quasars and the blazars. The blazars show a much weaker degree of correlation and the best fit line has a slope of around 0.5, while the non OVV quasars were highly correlated with a slope of 0.99. The next step is to convert the fluxes to luminosities and see how the correlations change.

Figure 14. The flux correlation diagram for the subsample TDO. The best fit line is shown and the correlation coefficient is given in the upper right of the diagram.

Figure 15. The flux correlation diagram for the TDWK subsample. This subsample includes all x-ray and observations that were made within one week of each other.

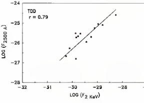
TDD
r = 0.79
-24
-25
-26
-27
-28
LOG (F2500 Å)
-32
-31
-30
-29
-28
-27
LOG (F2 KeV)

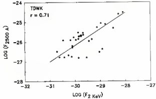
TDWK
r = 0.71
-24
-25
-26
-27
-28
LOG (F2500 Å)
-32
-31
-30
-29
-28
-27
LOG (F2 KeV)

Figure 16 The flux correlation diagram for the TD2WK subsample. This subsample contains all of the x-ray and optical observations that were made within two weeks of each other.

Figure 17. The flux correlation diagram for all observations of the BL Lacertid type sources.

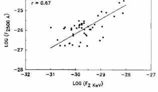
TD2WK
r = 0.67
-24
-25
-26
-27
-28
LOG ($F_{2500\ Å}$)
-32
-31
-30
-29
-28
-27
LOG ($F_{2\ KeV}$)

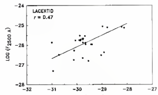
LACERTID
r = 0.47
-24
-25
-26
-27
-28
LOG ($F_{2500\ Å}$)
-32
-31
-30
-29
-28
-27
LOG ($F_{2\ KeV}$)

Figure 18 The flux correlation diagram for all observations of the sources which are classified as quasars

Figure 19 The flux correlation for all observations of quasars and lacertids combined

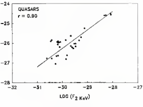
QUASARS
r = 0.80
-24
-25
-26
-27
-28
LOG (F2500 Å)
-32
-31
-30
-29
-28
-27
LOG (F2 KeV)

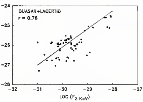
QUASAR+LACERTID
r = 0.76
-24
-25
-26
-27
-28
LOG (F2500 Å)
-32
-31
-30
-29
-28
-27
LOG (F2 KeV)

Figure 20. The flux correlation diagram for the sources classified as blazars. This sample includes both optically violent variable quasars and lacertids

Figure 21. The flux correlation diagram for the optically violent variable quasars.

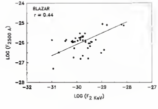
BLAZAR
r = 0.44
-24
-25
-26
-27
-28
LOG (F2500 Å)
-32
-31
-30
-29
-28
-27
LOG (F2 KeV)

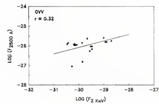
OVV
r = 0.32
-24
-25
-26
-27
-28
LOG (F2500 Å)
-32
-31
-30
-29
-28
-27
LOG (F2 KeV)

Figure 22. The flux correlation diagram for the non-optically violent variable sources

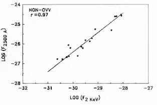
NON-OVV
r =0.97
−24
−25
−26
−27
−28
LOG (F2500 Å)
−32
−31
−30
−29
−28
−27
LOG (F2 KeV)

Luminosity Correlations

The conversion of fluxes to luminosities is described in Chapter II. The value of Hubble's constant was chosen as 55 Km/sec/Mpc and the value of q_0 is chosen to be 0.0. The lack of redshifts for some of the Lacertids prevented conversion of flux to luminosity. This reduced the sample size from 70 to 65 x-ray-optical pairs. The luminosity data are shown in Table 19. Column 1 of Table 19 lists the sources by name and column 2 gives the sequence number of the observation. The next two columns list the optical luminosity at 2500 angstroms and the 2 Kev x-ray luminosity. Column 5 gives the x-ray to optical slope as calculated by equation (2-14). The error in each quantity is shown in parentheses. The x-ray luminosity errors were calculated from the symmetric flux errors as discussed earlier.

The data listed in Table 19 are shown graphically in Figure 23. It is obvious from Figure 23 that the data are highly correlated and extend over five decades in x-ray and four decades in optical luminosity. The Bevington fit gives a smaller slope than the Jefferys method, 0.895(0.005) to 1.02(0.01). The correlation coefficient is 0.89, corresponding to a probability of no correlation of 1.4×10^{-8}. The correlation of the luminosity data is much more significant than the correlation of the entire flux sample presented in the previous section. The conversion to luminosity involves folding in the distance to each source, causing a redistribution in the $\mathrm{Log}(F_X)$-$\mathrm{Log}(F_O)$ plane. Figure 23 shows best fit lines to the data as calculated by the Jefferys method.

TABLE 19.
LUMINOSITY DATA

SOURCE	SEQ #	LOG(L_0)	LOG(L_X)	α_{OX}
0007+17	10125	29.59(0.05)	25.89(0.04)	1.42(0.03)
3C 66A	7725	31.29(0.06)	27.17(0.04)	1.58(0.04)
0235+16	5691	31.77(0.07)	28.07(0.07)	1.42(0.06)
0235+16	7506	31.07(0.08)	27.95(0.05)	1.20(0.05)
0235+16	7507	31.77(0.07)	28.28(0.06)	1.34(0.05)
0235+16	9283	30.93(0.04)	28.18(0.10)	1.06(0.05)
0235+16	9285	31.77(0.05)	28.32(0.03)	1.32(0.03)
0235+16	9562	31.77(0.05)	28.30(0.03)	1.33(0.04)
0420-01	2016	31.77(0.05)	28.73(0.07)	1.17(0.02)
3C 120	350	28.77(0.05)	25.82(0.03)	1.13(0.03)
3C 120	351	28.72(0.05)	25.63(0.03)	1.18(0.03)
3C 120	1939	28.72(0.05)	25.63(0.03)	1.18(0.03)
3C 120	4908	28.72(0.05)	25.58(0.03)	1.20(0.03)
3C 120	6389	28.93(0.06)	25.52(0.03)	1.31(0.04)
NRAO 190	2018	30.67(0.07)	27.45(0.09)	1.24(0.06)
0735+17	1991	31.10(0.06)	27.21(0.05)	1.48(0.04)
0735+17	1992	31.22(0.02)	27.06(0.06)	1.60(0.03)
0735+17	5695	31.21(0.05)	27.10(0.02)	1.58(0.03)
0735+17	7496	31.45(0.05)	27.10(0.04)	1.67(0.04)
0735+17	7497	31.30(0.02)	27.19(0.08)	1.58(0.04)
OI 363	3993	31.33(0.07)	27.21(0.07)	1.58(0.05)
0846+51	5228	31.36(0.06)	27.72(0.16)	1.40(0.08)
OJ 287	1993	30.75(0.09)	27.39(0.03)	1.30(0.04)
OJ 287	1994	30.74(0.07)	26.67(0.03)	1.56(0.03)
0906+01	2029	31.26(0.08)	27.68(0.09)	1.38(0.06)
MRK 421	5207	29.23(0.07)	26.06(0.09)	1.22(0.03)
3C 273	569	31.52(0.02)	27.95(0.03)	1.37(0.02)
3C 273	2037	31.44(0.07)	27.77(0.03)	1.41(0.04)
3C 273	5692	31.43(0.03)	27.71(0.03)	1.43(0.02)
3C 273	9310	31.47(0.04)	28.00(0.30)	1.35(0.02)
1308+32	5205	32.23(0.08)	28.15(0.04)	1.57(0.04)
OQ 172	2050	32.76(0.08)	29.11(0.08)	1.40(0.06)
OQ 172	2051	32.78(0.08)	28.91(0.09)	1.48(0.07)
1510-08	2053	30.60(0.03)	27.20(0.04)	1.31(0.03)
AP LIB	1997	29.09(0.10)	25.32(0.04)	1.45(0.05)
AP LIB	1998	29.11(0.05)	23.98(0.04)	1.97(0.03)
AP LIB	7493	29.26(0.03)	25.14(0.06)	1.58(0.03)
AP LIB	9647	29.26(0.03)	25.21(0.05)	1.55(0.03)
3C 345	2060	31.05(0.06)	21.76(0.04)	1.27(0.04)
3C 345	2061	31.29(0.05)	27.80(0.04)	1.34(0.03)
3C 345	5694	31.29(0.05)	27.84(0.03)	1.32(0.03)
3C 345	9261	31.15(0.07)	27.85(0.03)	1.27(0.04)
3C 351	510	30.90(0.06)	26.76(0.08)	1.59(0.05)
3C 351	2060	30.94(0.04)	26.67(0.07)	1.64(0.04)
3C 351	2063	30.99(0.07)	26.41(0.41)	1.76(0.06)
3C 351	4207	30.59(0.05)	26.97(0.06)	1.54(0.04)
3C 351	4208	30.93(0.07)	26.37(0.09)	1.75(0.06)

TABLE 19--CONTINUED

SOURCE	SEQ #	LOG(L_O)	LOG(L_X)	α_{OX}
3C 351	3688	30.87(0.03)	26.70(0.09)	1.60(0.06)
3C 351	5716	30.87(0.05)	26.67(0.03)	1.16(0.03)
3C 351	9378	30.90(0.08)	26.63(0.07)	1.64(0.05)
1727+30	2004	28.77(0.04)	26.23(0.03)	0.98(0.02)
1727+50	9389	28.63(0.06)	26.11(0.03)	0.97(0.03)
3C 371	1967	29.44(0.04)	23.30(0.06)	1.59(0.04)
OV 236	3890	31.53(0.04)	27.67(0.05)	1.48(0.03)
2128-12	8413	31.00(0.04)	27.48(0.03)	1.33(0.03)
2135-14	5426	30.38(0.03)	26.91(0.03)	1.33(0.03)
2155-30	3912	30.56(0.06)	27.37(0.02)	1.13(0.03)
2155-30	5201	30.63(0.04)	26.72(0.07)	1.50(0.04)
2155-30	5202	30.61(0.06)	27.47(0.03)	1.20(0.03)
2200+42	5693	30.17(0.03)	26.49(0.04)	1.41(0.02)
2201+31	7182	30.89(0.04)	27.35(0.04)	1.36(0.03)
2216-03	2068	31.59(0.09)	27.68(0.07)	1.50(0.06)
3C 446	8022	32.68(0.03)	28.64(0.05)	1.53(0.03)
2230+11	4042	31.33(0.03)	28.13(0.04)	1.23(0.24)
2345-16	2076	30.72(0.04)	27.17(0.09)	1.36(0.05)

Figure 23 The luminosity correlation diagram for all of the observations in Table 19

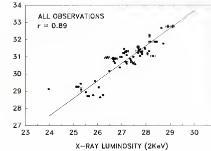
ALL OBSERVATIONS
r = 0.89
OPTICAL LUMINOSITY (2500 A)
X-RAY LUMINOSITY (2KeV)
27
28
29
30
31
32
33
34
23
24
25
26
27
28
29
30
31

The sample was divided, as in the previous section, to examine the characteristics of individual classes of objects and the effects of time delays on the correlations. Table 20 shows the correlation results for the total sample and the subsamples. The intercepts and slopes are from the Jefferys routine. Figures 24 through 32 show the correlation diagram for the subsamples with the best linear fit for each one.

TABLE 20.
LUMINOSITY CORRELATIONS

TYPE	N	INTERCEPT	b	r	PROBABILITY OF NO CORRELATION
ALL	65	3.0(0.2)	1.02(0.01)	0.89	4.09×10^{-8}
TDO	11	10.1(0.5)	0.77(0.02)	0.92	6.01×10^{-5}
TDWK	29	1.8(0.4)	1.07(0.02)	0.90	3.95×10^{-8}
TD2WK	43	5.3(0.3)	0.94(0.01)	0.89	4.06×10^{-8}
LACERTID	27	6.3(0.3)	0.90(0.01)	0.76	4.42×10^{-6}
QUASAR	31	8.7(0.5)	0.82(0.02)	0.86	4.13×10^{-8}
QSO+ LACERTID	58	6.4(0.3)	0.90(0.01)	0.88	5.52×10^{-8}
BLAZAR	42	6.8(0.4)	0.88(0.01)	0.62	1.00×10^{-5}
OVV	20	-0.2(0.5)	1.14(0.02)	0.93	1.40×10^{-8}
NON-OVV	18	1.2(0.4)	1.09(0.01)	0.95	2.30×10^{-9}

The first line in Table 20 lists the fit parameters for all of the luminosity data from Table 19. When luminosities are used instead of fluxes, the correlation coefficient increases from 0.74 to 0.89. The increase occurred because the points are redistributed when the redshifts are folded in. The dynamic range of the observations in luminosity is a factor of 100 greater than in flux. This spreads the points out and also tends to increase the correlation for a fixed number of points. The slope is very close to 1.0.

Figure 24. The luminosity correlation diagram for the all of the simultaneous observations.

Figure 25. The luminosity correlation diagram for all x-ray and optical observations that were made within one week of each other

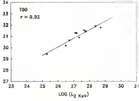
TOO
r = 0.92
LOG ($L_{2500\,Å}$)
LOG ($L_{2\ KeV}$)
34
33
32
31
30
29
28
27
23
24
25
26
27
28
29
30
31

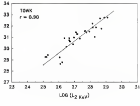
TOWK
r = 0.90
LOG ($L_{2500\,Å}$)
LOG ($L_{2\ KeV}$)
34
33
32
31
30
29
28
27
23
24
25
26
27
28
29
30
31

Figure 26 The luminosity correlation diagram for the TD2WK subsample

Figure 27 The luminosity correlation diagram for the lacertid observations

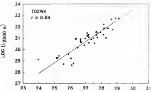
T02WK
r = 0.89
LOG (L2500 Å)
LOG (L2 KeV)
34
33
32
31
30
29
28
27
23
24
25
26
27
28
29
30
31

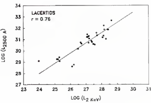
LACERTIDS
r = 0.76
LOG (L2500 Å)
LOG (L2 KeV)
34
33
32
31
30
29
28
27
23
24
25
26
27
28
29
30
31

Figure 28. The luminosity correlation diagram for only the quasars.

Figure 29. The luminosity correlation diagram for all quasars and all lacertids combined.

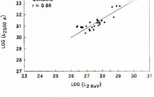
QUASARS
r = 0.86
LOG (L2500 Å)
LOG (L2 KeV)
34
33
32
31
30
29
28
27
23
24
25
26
27
28
29
30
31

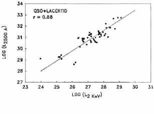
QSO+LACERTID
r = 0.88
LOG (L2500 Å)
LOG (L2 KeV)
34
33
32
31
30
29
28
27
23
24
25
26
27
28
29
30
31

Figure 30 The luminosity correlation diagram for the BLAZAR subsample

Figure 31. The luminosity diagram for the optically violent variable quasars

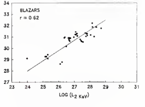
BLAZARS
r = 0.62
LOG (L$_{2500\ Å}$)
LOG (L$_{2\ KeV}$)
34
33
32
31
30
29
28
27
23
24
25
26
27
28
29
30
31

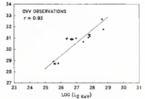
OVV OBSERVATIONS
r = 0.93
LOG (L$_{2500\ Å}$)
LOG (L$_{2\ KeV}$)
34
33
32
31
30
29
28
27
23
24
25
26
27
28
29
30
31

Figure 32 The luminosity diagram for the non-optically violent sources only

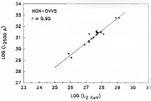
NON-OVVS
r = 0.95
LOG (L2500 Å)
LOG (L2 KeV)
34
33
32
31
30
29
28
27
23
24
25
26
27
28
29
30
31

The second line shows an improved correlation in the simultaneous data, although not nearly as significant as for the entire sample. The TOO sample is dominated by Lacertids and OVV quasars which show less correlation than more optically quiescent sources. The time delay between variations in the x-ray and optical light curves of active quasars may work to destroy the simultaneous correlations.

The TDWK sample contains more non OVV quasars and the elliptical galaxy MRK 421. The correlation increases in significance and the slope increases to 1.07. Finally, the TD2WK sample is slightly less significant than the TDWK sample and the slope flattens slightly to 0.94. These differences may be insignificant, but the data establish a slope near 1.0 with a high degree of correlation for all of the sources in the sample, regardless of time delay.

Examining the results for the other classes of objects, the blazars exhibit significantly more scatter than the non OVV sample. The BLAZAR and LACERTID samples both show slopes around 0.9 and correlation coefficients smaller than 0.76. The OVV sample, on the other hand, shows a high degree of correlation with a correlation coefficient of 0.93. This is in complete contrast to the results for the flux correlations where the OVV's showed the least amount of correlation.

The NON-OVV sample continues to show a remarkable degree of correlation. The correlation coefficient of 0.95 is similar to the correlation coefficient seen with the fluxes.

There seems to be some difference between the slopes for quasars (0.82) and Lacertids (0.90). All of the slopes found in these correlations are steeper than the values published by Blumenthal, Keel and Miller (1982) and Tananbaum et al. (1983).

Tucker (1983) calculated the dependence of the x-ray luminosity on the optical luminosity for a thick disk accretion model and for a relativistic wind model. He determined that the x-ray luminosity is a function of the optical luminosity to the 0.75 power in the thick disk case. The exponent is more like 0.49 in the case of the relativistic wind. The observations here do not agree with either model. Multiple sources of x-ray emission could account for some of the differences.

X-Ray Optical Spectral Indices

Values for the x-ray-optical spectral index quoted in the literature range from 1.27 to 1.50. The results of Ku, Helfand and Lucy (1980) indicated that radio-quiet and radio-loud quasars have α_{ox}'s of 1.5 and 1.35 respectively. The observations in Table 19 indicate that α_{ox} can range from 0.97 (1727+50) to 1.76 (3C 351). For all of the sources, the average α_{ox} is 1.62 with a standard deviation of 0.22. The Lacertids have a mean α_{ox} of 1.57(0.26) and the quasars have a mean of 1.59(0.13). The non-OVV sources have a mean around 1.59 with a standard deviation of 0.1. Quasars as a group are not distinguishable from Lacertids by their mean x-ray-optical spectral index, although non-OVV quasars tend to have a much smaller α_{ox}.

The three types of spectral indices α_o, α_x, and α_{ox} are compared in Table 21 for three kinds of AGN. Only those objects whose x-ray spectra were adequately fit with a power-law model are included in Table 21. The first column indicates the type of source, while the second column lists the number of objects included in the sample. The next three columns list the mean spectral indices for each type of source.

TABLE 21.
COMPARISON OF MEAN SPECTRAL INDICES

TYPE	N	α_o	α_x	α_{ox}
SEYFERT	2	1.53(0.32)	1.44(0.08)	1.50(0.15)
QUASARS	6	0.55(0.36)	0.75(0.55)	1.61(0.21)
LACERTIDS	7	1.67(0.89)	1.57(0.44)	1.56(0.21)

The Seyferts and Lacertids have similar optical and x-ray spectral indices, while the spectral indices of the quasars are much lower. These results agree with previous findings (Urry *et al.* 1986). Although there is large dispersion, the x-ray spectral index for Seyfert galaxies and Lacertids is larger than the canonical value of 0.5. One quasar, OV-236, has an x-ray spectral index of 1.81, but the remainder are below 0.9. Only one of the 7 Lacertids, 1727+50, shows an x-ray spectral index below 1.5. This indicates that the canonical value for the x-ray spectral index of Lacertids and Seyferts is closer to 1.6 than 0.5. The average α_{ox}'s for all three types of sources are similar and consistent with 1.6.

Correlations with luminosity ratio

Tananbaum *et al.* (1979) and Zamorani *et al.* (1981) suggested a correlation between the x-ray optical luminosity ratio and optical luminosity. The possibility of this type of correlation was tested in all of the subsamples in this work. The log of the optical luminosity was treated as the independent variable and the log of the luminosity ratio was the dependent variable.

The total luminosity sample exhibited a weak inverse correlation with $r = -0.45$ with a probability of 1.7×10^{-4} of arising by chance. Of the subsamples, only the QUASAR+LACERTID subsample showed a strong positive correlation, with a correlation coefficient of 0.62. The probability of an uncorrelated sample showing a correlation this high is 2.6×10^{-7}. The general lack of correlation in the other subsamples, $r_{avg} = 0.35$, and the small correlation coefficient in the QUASAR+LACERTID subsample indicates the correlation may only be statistical. Zamorani et al. (1981) found a positive correlation between luminosity ratio and optical luminosity, but Avni and Tananbaum (1983) argue that the correlation is only fortuitous and not a real physical correlation.

Correlation coefficients between the luminosity ratio and redshift were also calculated for each subset. The uneven redshift distribution of the total sample implies low statistical reliability on any correlations found. This problem was even more severe for the individual subsamples. The distribution of the main sample in redshift vs. the spectral index α_{ox} is shown in Figure 33. The average correlation coefficient was 0.39, but the majority were anti-correlations. Previously published correlations between the luminosity ratio (equivalent to α_{ox}) and redshift imply that if the correlation does exist, it must be an inverse correlation. In other words, as the

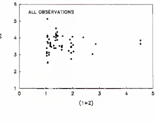

Figure 33 The x ray-optical spectral index α versus (1+z) for all of the sources in Table 3.

redshift increases, the luminosity ratio decreases. The most significant correlation found in the subsamples was -0.92 with a probability of 6.02×10^{-5}. This was with the TDO subsample. The total sample yielded a positive correlation with a correlation coefficient of 0.44.

The statistics of these correlations are still inadequate because of the concentration of low redshift quasars in this sample. A larger and more uniformly distributed sample in redshift is required in order to settle the question of spatial and/or luminosity evolution in AGN.

The X ray Background

Study of the extragalactic x-ray background was begun in 1962 by Giacconi _et al._ (1962). Boldt and Leiter (1984) approximated the spectrum of the x-ray background by the expression

$$dI = AE^{\theta}\exp(-E/kT)dE, \qquad (3\text{-}20)$$

where E is in KeV, A is 5.6 KeV/(Kev-cm^2-sec-str), kT is 40 KeV and θ is 0.29. Previous background studies by De Zotti _et al._ (1982), Schmidt and Green (1983), Schmidt and Green (1986), and Boldt and Leiter (1984) show AGN make up as much as 70% of the total x ray background at 2 KeV. The x-ray background calculation depends on the x ray-optical spectral index α_{ox}. The value of α_{ox} commonly used in these calculations is 1.5, which agrees with the average α_{ox} found here. Therefore, the previously reported percentage of the 2 KeV x-ray background made up by AGN is not changed by the results found here.

The difference between the average AGN spectral index and the background spectral index is a more severe problem than the total x-ray flux contribution of AGN's. The index is 0.29 for the background, but either 0.7 for quasars or 1.5 for Lacertids. The larger value of 1.5 for Lacertids increases the difficulties in accounting for the shape of the background spectrum by known point sources. The precursor AGN which have been postulated to explain the background spectrum must have a harder spectrum than previously anticipated.

Primary Conclusions from Correlations

The primary results found in the correlation studies presented in this chapter are:

1. The flux data are highly correlated, with the non-ovv sources exhibiting a correlation coefficient of 0.97. The Blazar and OVV subsamples are the least correlated, r = 0.44 and 0.32 respectively.
2. The slope of the best fit lines to the flux data subsamples are between 0.75 and 0.99.
3. When the data are converted to luminosity, the significance of the correlations increases. The correlations for the OVV quasars and the Blazars become significant when the luminosity data are used instead of the flux data. The slopes of the fits range from 0.77 to 1.14.

with the simultaneous observations being the flattest and the OVV quasars the steepest.

4 The average x-ray to optical spectral index for all sources in this sample is 1.56, with a mean dispersion of 0.16. This value agrees with previously deduced values and does not change background predictions.

5 The average x-ray spectral index for Lacertids is 1.57 as compared to quasars, whose index is only 0.75. This result agrees with previous spectral fits of Lacertids (Urry *et al.* 1986). The dispersions, however, are high and the significance of this finding awaits more x-ray observations of lacertids

CHAPTER IV
INDIVIDUAL SOURCE STUDY

Introduction

The construction of multifrequency spectra is an approach commonly used to investigate the emission properties of active galactic nuclei. This approach requires data in other frequency bands in addition to x-ray and optical observations. Nearly simultaneous multifrequency spectra for a number of AGN have been analyzed by Bregman *et al.* (1981), Bregman *et al.* (1986a), Bregman *et al.* (1986b), and Jones, Rudnick and Landau (1986). Urry (1988) gives an excellent summary of multifrequency observations of blazars, complete with references.

In a study of this type, the primary consideration is to construct a spectral distribution of an individual object with simultaneous observations at as many frequencies as possible. Obtaining complete spectral coverage is extremely difficult because each frequency band requires different detectors operated independently, some of which must be located on satellite platforms in order to place the detector above the atmosphere. An example of a particularly successful attempt to coordinate telescopes sensitive to frequencies extending from the radio region up to x-rays is reported in Bregman *et al.* (1986a). In this work, Bregman obtained simultaneous observations at 23 frequencies between 10^9 (radio) and 10^{18} Hz (x-ray).

Once a fairly complete spectrum has been obtained, emission models of the source can be constructed. The most successful models for interpreting the multifrequency spectra of AGN are synchrotron self-Compton models (hereafter SSC). There are two basic versions of the SSC model, one formulated for plane parallel geometry (Jones, O'Dell and Stein 1974, hereafter JOS), the other for spherical geometry (Blumenthal and Gould 1970). Other more complex SSC models include more complex geometries and relativistic motion or streaming. These "jet models" have a fundamental drawback in that they require specification of the radial dependencies of the magnetic field. This additional parameter cannot at present be derived from observations, so the model is under constrained.

Synchrotron Self-Compton Models

In the following sections, we will discuss briefly the synchrotron and Compton emission processes, and then present the particular SSC model to be used in the discussion of the multifrequency spectra.

Basic Synchrotron Theory

Alfven and Herlofson (1950) first considered the importance of synchrotron radiation in astronomical sources. Successful synchrotron models have been constructed for such diverse astronomical phenomena as radio emission from planets, supernovae, and pulsars. The characteristic non-thermal spectrum and the high degree of polarization seen in these sources are signatures of the synchrotron process.

When a charged particle moves perpendicular to an external magnetic field, the particle experiences an acceleration orthogonal to both the direction of the magnetic field lines and the particle velocity. The resulting spiral path has a radius of

$$R = \frac{m\ v}{e\ B} \qquad (4\text{-}1)$$

where R is the radius of the spiral path, m is the mass of the particle, v is the particle velocity, e is the charge, and B is the external magnetic field strength. The cyclotron or gyro frequency ω is given by

$$\omega = \frac{v}{2\ \pi\ R} = \frac{e\ B}{2\ \pi\ m} \quad \text{cps} \qquad (4\text{-}2)$$

If the particle is moving relativistically, the radiation is concentrated in a cone of angle θ_c, where θ_c is the equal to twice the Lorentz factor of the electrons which is $(1+v^2/c^2)^{½}$.

An ensemble of electrons that has a power-law distribution in energy is given by,

$$N(E) = C_1\ E^{-a}, \qquad (4\text{-}3)$$

where N(E) is the number of particles per unit energy E, C_1 is a constant and a is the spectral index. The total power radiated is given by equation (4-4)

$$W = C_1 \int E^2\ E^{-a}\ dE = C_2\ E^{3-a} \qquad (4\text{-}4)$$

Since the highest frequency emitted by an electron is proportional to the square of its energy, the total power can be written as

$$W = C_2 \, f^{\frac{1}{2}(3-e)} \qquad (4\cdot5)$$

Differentiating equation (4·5) as a function of frequency and including the dependence on the magnetic field strength, we obtain the total power radiated by an assemblage of relativistic electrons in a magnetic field B is

$$S = C_3 \, f^{\frac{1}{2}(1-e)} \, B^{\frac{1}{2}(e+1)} \qquad (4\cdot6)$$

The resulting optically thin synchrotron spectrum is a power law in frequency with the spectral index α and the index of the electron distribution e related by the expression $\alpha = \frac{1}{2}(1-e)$.

An important frequency in the synchrotron spectrum is the frequency at which the synchrotron source becomes optically thick, i.e., the self-absorption frequency. The synchrotron absorption coefficient a_f is proportional to $f^{-\frac{1}{2}(e+4)}$, so the optically thick source function is then given by

$$S_t = \frac{S}{a_f} = C_4 \, f^{5/2} \qquad (4\ 7)$$

The spectral index for a power law distribution of relativistic electrons below the self-absorption frequency goes as frequency to the 5/2 power. The self absorption frequency can be identified in the synchrotron spectrum as the frequency where the $f^{5/2}$ spectrum turns over and becomes a power law of the form $f^{-\frac{1}{2}(1-e)}$. Another feature in the synchrotron spectrum occurs at high frequencies where radiative losses of the highest energy electrons cause a break or steepening of the power law. An example of the synchrotron spectral distribution is shown in Figure 34.

Compton Interactions

In compact synchrotron sources where the photon energy density is sufficiently high, the relativistic electrons collide with the synchrotron photons and some of the electron's energy is transferred to the photon. This process, inverse Compton scattering redistributes some of the synchrotron photons to higher frequencies, thus altering the observed synchrotron spectrum.

Compton scattering is the relativistic counterpart of Thomson scattering. As a result of quantum effects, the kinematics of the scattering process change and the cross section for scattering changes with energy. The wavelength of the scattered photon changes by a factor equal to the Compton wavelength, 0.02426 Angstroms for electrons. The differential cross-section is given by the Klein-Nishina formula which, in the extreme relativistic regime, is

$$\sigma = 0.275\sigma_T x^{-1}(\ln(2x)+0.5), \qquad (4\text{-}8)$$

where $x = hf/mc^2$ and σ_T is the Thomson cross section.

The amount of energy transferred by a single electron to a photon in one scattering is proportional to γ^2, where γ is the electron energy

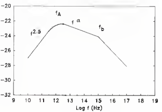

Figure 34. The spectral distribution shown above results from a power law distribution of relativistic electrons moving in an external magnetic field. The portion of the spectrum where the flux increases as $f^{2.5}$ is the optically thick emission. The point where the spectrum turns over, f_A is the turnover frequency or self-absorption frequency where the optical depth is equal to unity. The optically thin portion of the spectrum goes as $f^{-\frac{1}{2}(s-1)}$. The break frequency, f_b, occurs because high energy electrons lose energy more rapidly than the low energy electrons.

in units of mc^2. The power in the Compton radiation is given by

$$P_{comp} = 0.275\sigma_T c\gamma^2\beta^2 U_{ph} \qquad (4.9)$$

In equation 4-9, β is $(1-v^2/c^2)^{-1}$, c is the speed of light, γ is the electron energy, and U_{ph} is the energy density of photons. It is obvious from equation (4-9) that the more compact a bright synchrotron source is, the larger the Compton emission will be. The small dimensions and extremely large luminosities of AGN lead to the "Compton catastrophe". A simple expanding source synchrotron model can easily explain the radio emission seen in most AGN, but when this simple model is used to explain the optical emission, the predicted Compton flux (which will be in the x-ray frequency band) is usually larger than the observed x-ray emission. The usual method to circumvent the Compton catastrophe is to invoke relativistic bulk motion which alleviates both the size restriction and decreases the luminosity. Both factors lower the photon energy density, thus lowering the Compton emission.

The SSC Model

Blumenthal and Gould (1970) examine in detail the resulting spectrum from relativistic electrons in a magnetic field losing energy by synchrotron, bremsstrahlung, and Compton processes. Urry (1984) gives corrected and consistent formulae for synchrotron self Compton sources using both Blumenthal and Gould's and Jones, O'Dell and Stein's formalisms. We have used the Jones, O'Dell and Stein formalism as given by Urry (1984). The important parameters in the SSC equations are defined as

f_A — the self-absorption (turnover) frequency in gigahertz,

f_b — the frequency at which the optically thin spectrum steepens due to δ^2 losses (break frequency) in units of gigahertz,

F_A — flux density in Janskys at the self-absorption (turnover) frequency,

θ_e — the angular diameter of the source in milliarcseconds,

E — the energy at which the Compton flux is desired in KeV,

D — the distance to the source in gigaparsecs,

z — the redshift of the source,

α — the optically thin spectral index of the synchrotron spectrum

δ — The kinematic Doppler factor

The expression for the magnetic flux density is given in terms of the self-absorption frequency f_A, the flux density F_A at the self-absorption frequency, and the angular size of the emitting region

$$B = 4.04\times10^{-3} b_{x\alpha}{}^{2}\theta_e{}^{4} f_A{}^{5} F_A{}^{-2}[\delta/(1+z)] \qquad (4\text{-}10)$$

In equation (4-10) the parameter $i_{\alpha 0}$ is a dimensionless function of the spectral index whose values are tabulated in Jones, O'Dell and Stein (1974) and Urry (1984). The electron number density is given by

$$N_0 = (0.42)(5.9\times10^{8})^{\alpha} i_{\alpha 0}^{-2\alpha-2} j_{\alpha 0}^{-1}$$
$$\times\ \theta_0^{-4\alpha-7} f_A^{-4\alpha-5} F_A^{2\alpha+3} D^{-1} (1+z)^{2\alpha+6} \delta^{2\alpha-4} \qquad (4\text{-}11)$$

The parameter $j_{\alpha 0}$ in equation (4-11) is another dimensionless quantity given in Urry (1984) and D is the distance to the source. The number density is given in units of $\mathrm{ergs}^{2\alpha}\text{-}\mathrm{cm}^{-3}$ and can be converted to number/cm^3 by dividing by the energy of the electrons at the turnover frequency in ergs to the 2α power. The expected flux F^{sc} due to Compton scattering at energy E is given by

$$F^{sc} = (4.14\times10^{-6})(3.66\times10^{4})^{\alpha} e_{\alpha 0} i_{\alpha 0}^{2\alpha-2}$$
$$\times\ \ln(f_b/f_A)\ \theta_0^{-4\alpha-6} f_A^{-3\alpha-5} F_A^{2\alpha+4}$$
$$\times\ E^{-\alpha}\{(1+z)/\delta\}^{2\alpha+4} \qquad (4\text{-}12)$$

The dimensionless function $e_{\alpha 0}$ is tabulated in JOS. The self-Compton flux at energy E (in KeV) is given in units of Janskys in equation (4-12). Ideally, the observable quantities in the above equations θ, α, f_A, F_A, z, D, and f_b, can be estimated from observations of the multifrequency continuum spectrum, the optical line spectrum and variability characteristics. Unfortunately, because of the difficulties in obtaining accurate simultaneous observations in the infrared, millimeter and far ultraviolet range, the values of some of the parameters are difficult to estimate precisely.

Before presenting the actual multifrequency spectra, relativistic bulk motion or beaming will be briefly discussed. The kinematic Doppler factor δ in the SSC equations is initially set to 1. The kinematic factor describes the degree of relativistic motion in the emitting region and is equal to $(\Gamma(1-(v_c/c)\cos\Phi))^{-1}$. The v_c is the non-cosmological velocity of the emitting source, c is the speed of light, Γ is the Lorentz factor, and Φ is the angle between the motion of the source and the line of sight. If the predicted Compton flux is larger than the observed x-ray flux at that frequency (the Compton catastrophe), the Doppler factor can be increased until the model prediction agrees with the observations. The justification for including this extra parameter is based upon observations that many AGN eject plasma jets, some of which seem to be moving at relativistic speeds. These superluminal sources, usually studied at radio frequencies, present evidence that there is a preferred direction in which ejecta are accelerated. Begelman, Blandford and Rees (1984) give an excellent comprehensive review of the theory and cite evidence for relativistic jets in AGN. Many previous multifrequency studies of Lacertids require bulk relativistic motion to account for the lack of self-Compton flux (Urry 1984; Worrall 1986).

Multifrequency Observations

The observations from Chapter II, complimented with data from the literature, are used to construct multifrequency spectra for each source. The basic method adopted here was to construct additional optical and infrared points in the multifrequency spectrum from the optical data in Table 3 and average optical and near-infrared spectral indices for each source. Obviously direct observations in each of the frequency bands are preferable to using average spectral indices to estimate the flux in each band. Since in the majority of cases no color data were available, we have resorted to this approximation. Although there are exceptions, variability studies show that the optical-near-IR spectral region varies in unison, keeping nearly the same spectral shape. We are not concerned here with small variations between closely spaced spectral bands, rather the broad variations over several decades in frequency.

The parameters of the SSC model are estimated from the spectrum by the following method. The frequency and flux density at the self-absorption turnover point are estimated by extrapolating a line through the near-IR and far IR data until it intersects with a linear extrapolation of the radio data. The point of intersection should be near the turnover frequency. This assumes that the IR flux represents the optically thin synchrotron emission and the slope of the linear fit to the IR data is the optically thin spectral index α.

In some spectra (0235+164), a sharp spectral break occurs in the optical-near-IR bands which can be attributed to the break in the synchrotron spectrum. In other sources no such obvious break occurs, as the break frequency must fall in the unobserved ultraviolet band. The lack of a distinct break feature in some spectra does not significantly effect the results since the Compton flux depends only on the natural log of the ratio of the break frequency and the turnover frequency. If the break frequency is 10^{16} instead of 10^{14} Hz, the Compton flux estimate changes by 25%, whereas errors of only a factor of 5 in estimating the turnover frequency change the Compton flux by 21% (if a = 0.6). The primary function of the break frequency is to calculate the high energy electron distribution cutoff E_{max}, which depends on the square of the break frequency.

The angular size is an important quantity which cannot be estimated from the multifrequency spectra. Not even the most sensitive VLBI radio observations with angular resolutions down to one millisecond have been able to resolve the compact core components of these sources. We use the minimum variability timescale to estimate the maximum size of the emitting region. The minimum variability timescales for four of the six sources studied here are obtained from the work of Pollock (1982). Minimum variability timescales for the other two sources were estimated from the RHO data using the method described by Pollock (1982). These timescales were then converted to linear diameters by the relation:

$$D < \frac{4c\, dT\, L_{avg}}{3.14(1+z)\, dL} \qquad (4\text{-}13)$$

In equation (4-13), c is the speed of light, z the redshift of the source, dT the minimum variability timescale in days, L_{avg} the average luminosity during the variation, and dL is the maximum change in luminosity. The linear diameter D of the emitting region is in units of light days. This diameter is then converted to angular size by the expression, $\theta_e = D/2d$, where d is the distance to the source.

Finally, the x-ray flux at 2 KeV provides an upper limit to the Compton emission. Instead of solving directly for the Compton flux through equation (4-12), we chose to compute the Doppler boost factor δ, using the flux at 2 KeV as an upper limit to the Compton flux.

The remaining SSC equations are solved using the estimated parameters and the δ calculated from equation (4-12). A brief discussion of the individual sources, addressing the assumptions necessary to estimate the SSC parameters, is given below.

0235+164

The multifrequency spectrum of 0235+164 has been studied by Brown et al. (1988) and Impey and Neugebauer (1988). Radio observations from Aller et al. (1985) and IRAS (InfraRed Astronomical Satellite) data from Impey and Neugebauer (1988) have been combined with the x-ray and optical data presented in Chapter II. Additional data points in the infrared-optical portion of the spectra have been calculated using the 2500 angstrom flux from Table 3 and spectral indices from Brown et al. (1988), Webb and Smith (1988), O'Dell et al. (1977), and Smith (1986). The shape of the optical-IR spectrum is concave downward, but can be adequately approximated by a broken power law. The IR power law has a slope of -1.6, while the steeper optical power law has a slope of -3.9. The optical-IR spectral shape of 0235+164 is generally retained as the brightness level increases or decreases over a range of several magnitudes. Spectral changes have been reported by Brown et al. (1988) but these changes will be neglected here as we are interested only in the broad character of the spectrum. All optical and infrared data have been differentially reddened to account for the high hydrogen column density indicated by the x-ray observations (see Chapter II).

The IRAS observations were made nearly three years after the x-ray observations. Rosemary Hill optical observations coincident with the IRAS observations were 0.58 magnitude fainter than the optical brightness during the x-ray observations. Impey and Neugebauer (1988) studied a number of blazars and found the flux density variations in the IRAS sensitive spectral bands are smaller by at least a factor of two than the variations seen in optical flux densities. They also found that 0235+164 exhibited no variability in IRAS observations, however only two observations which were taken fourteen days apart were used to form this conclusion. The largest optical variation on that timescale is a factor of three, so if the far-infrared fluxes are variable at all they probably vary only by a factor of 1.5. Errors in this assumption will cause errors in the optically thin spectral index and, more importantly, errors in determining the turnover frequency. Variation in the spectral index from 0.0 to 1.4 causes a variation in the resulting Doppler boost factor by only 1.117. In order to account for variances in these parameters, results will be quoted for a range of possible turnover frequencies.

The break between the optical and near-infrared bands is interpreted here as the break frequency in the SSC models. The turnover frequency and flux are found by the intersection of linear fits through the radio and infrared data. An example of the multifrequency spectral distribution of 0235+164 is shown in Figure 35.

0735+17

Five multifrequency spectra of 0735+17 were constructed, one corresponding to each x-ray observation. Additional spectral coverage was obtained by adding contemporaneous radio observations from Aller *et al.* (1986) and IRAS observations from Impey and Neugebauer (1988). Near infrared and optical data are calculated from average spectral indices from Brown *et al.* (1988) O'Dell *et al.* (1978), and Bregman *et al.* (1984). O'Dell found that the spectrum from 0.36 microns to 3.5 microns is adequately modelled by a continuous power law with a spectral index of 0.75. Brown found the spectral index varied between 0.7 and 3.3, with an average value of 0.9. Two IRAS observations of 0735+17 were made when its optical brightness was B = 15.65 and B = 15.47 magnitudes respectively. The optical brightness of 0735+17 during the x-ray observations was between B = 15.41 and B = 15.80, with an average of B = 15.62. The IRAS observations indicate the flux is marginally variable with an amplitude five times smaller than optical variations over the same timescale. When the optical magnitude during the x-ray observation is brighter than B = 15.5, the IRAS observation of 11/14/83 is used, since the optical brightness on that date was B = 15.47. When the optical brightness during the x-ray observation is fainter than 15.5, the IRAS observations of 10/13/83 are used.

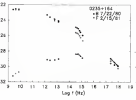

Figure 35. The multifrequency spectral distribution of AO 0235+164. The filled circles are the flux densities and the filled triangles represent the energy at each frequency, both for the 7/22/80 observation. The dotted lines are best fit lines to the infrared and radio data respectively. The slope of the line through the infrared data is the optically thin synchrotron spectral index. The intersection of the two lines defines the best fit turnover frequency and the corresponding self-absorption flux density. The open circles are the data from 2/15/81. The variations in the optical flux level define a different spectral index and turn over frequency for this observation. The other four multifrequency spectra are indistinguishable from the 7/22/80 spectrum. The solid lines through the x-ray data show the uncertainty in the x-ray spectral index. Error bars are included if they are larger than the symbol size.

The ultraviolet spectral distribution becomes steeper beyond 2500 angstroms, possibly corresponding to the break frequency in the synchrotron spectrum. The multifrequency spectrum of 0735+17 is shown in Figure 36.

OJ 287

Average values of 0.96 and 0.98 were used for the near-infrared and optical spectral indices respectively (Smith 1986 and Brown et al. 1988). These spectral indices are appropriate when the optical flux level is similar to the flux level seen during the x-ray observations.

The far-infrared (IRAS) observations provided a difficult problem. The IRAS observations were made when the optical brightness was about one magnitude brighter than the optical brightness during the x-ray observations. The IRAS data implied variability in the far-infrared flux, although the amplitude of the variations may be much smaller than corresponding variations in the optical flux. There is no clear way of determining the proper far-infrared flux density appropriate for fainter optical flux densities. We used the published IRAS data with the stipulation that possible far-infrared fluctuations could cause errors in the determination of the turnover frequency and the optically thin spectral index. We have computed a number of models assuming a range of turnover frequencies to account for these errors. Figure 37 shows the multifrequency spectral distribution of OJ 287.

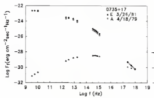

Figure 36. The multifrequency spectrum of 0735+17 is shown above for the date 3/26/81. As in Figure 35, the filled triangles represent the energy at each frequency and the filled circles indicate the flux density. The dotted lines represent linear extrapolations of the infrared and radio data. The intersection of these lines is taken to be the turnover flux density and frequency. The turnover frequency at $10^{11.5}$ is consistent with the multifrequency spectra of Impey and Neugebauer (1988). The curvature of the optical data suggests a break at $10^{14.7}$. The open circles represent the flux densities on 4/18/79. The differences between these and the 3/26/81 is due to variability.

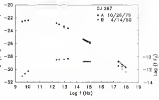

Figure 37 The multifrequency spectral distribution of OJ 287 is shown for the date 10/26/79 The far-infrared data are not simultaneous as described in the text The filled circles represent the flux at each frequency while the filled triangles represent a measure of the energy at each frequency The dotted lines indicate the best fit linear extrapolations of the infrared data and radio data The intersection is used to estimate the turnover frequency The open circles represents the multifrequency spectrum of 10/17/79 The only perceptable change was in the x-ray flux

3C 273

Landau *et al.* (1986) give the near-infrared spectral index for 3C 273 as -1.3. This infrared index and the optical index from Table 3 were used to extend the spectral coverage shown in Figure 38. The flat optical spectral distribution is generally interpreted as a thermal component, possibly emission from an accretion disk. The optical points were excluded from the calculation of the optically thin x-ray spectral index because of the possible thermal origin of the radiation.

Only one set of IRAS observations was available for this source (Impey and Neugebauer 1988). Since no variability information in the far-infrared is available and optical variations for 3C 273 are of modest magnitude, we have assumed the IRAS observations are representative of the far-infrared flux density during the x-ray observations.

AP LIBRAE

The near-infrared spectral index of AP Librae was given by Allen, Ward, and Hyland (1982) as 0.82. We have used this infrared spectral index and the optical spectral index from Table 3 to extend the multifrequency spectral coverage. The RHO optical light curve shows the optical brightnesses during the x-ray and IRAS observations were different by about one magnitude. Given the assumption that the amplitude of variability decreases toward longer wavelengths, we use the IRAS data with the proviso that any variations in the far-infrared data might change the turnover frequency.

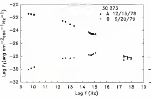

Figure 38. The multifrequency spectrum of 3C 273 is shown for the date 12/13/78. The filled triangles represent the energy at each frequency and the filled circles show the flux at each frequency. The dotted lines are linear fits to the infrared data and radio data. The intersection of the lines is taken to be the location of the turnover frequency. The flat optical distribution represents the blue bump. This blue bump is usually attributed to thermal emission, possibly from an accretion disk. Because of the possible thermal origin of the optical points, they were not used to estimate the optically thin spectral index or the self absorption frequency. The open circles represent the flux densities on 10/17/79.

The sharp break between the near-infrared and the optical bands is interpreted as the synchrotron break frequency and is included in the models. The multifrequency spectral distribution of AP Librae is shown in Figure 39.

3C 345

The mean near-infrared spectral index of -1.5 is used for this source although variations of 0.5 have been seen (Brown 1988). The slight flattening of the optical spectrum is probably due to the presence of a thermal component.

Several IRAS observations were available for this source. We selected an IRAS observation to use with each x-ray optical observation based on the optical brightness of the source during the observations. This procedure was described earlier in reference to 0735+17.

Bregman et al. (1986) presented a remarkably complete multifrequency spectrum of 3C 345. Their observations indicated that the break frequency probably lies in the 10^{15}-10^{16} Hz range. The multifrequency spectrum of 3C 345 is shown in Figure 40.

Model Results

The results of the SSC models for all of the multifrequency spectra are presented in the following tables. Each spectrum of each source is labeled alphabetically beginning with A in chronological order.

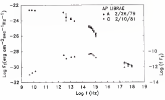

Figure 39 The multifrequency spectrum of 2/26/79 is presented for AP Librae. The filled triangles represent the energy at each frequency and the filled circles represent the flux. For AP Librae, the break frequency is obvious at $10^{14.8}$ and is extrapolated to high frequencies with a dotted line. The other two dotted lines are best fit lines to the radio fluxes and infrared fluxes. The intersection of these two lines are used to estimate the turnover frequency and flux density best fit parameters for each spectrum are compared and then the results of the allowed ranges of variation for the turnover frequency are presented for each source. The open triangles represent the multifrequency spectrum for 2/10/81.

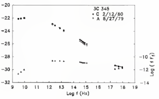

Figure 40. The multifrequency spectral distribution of 3C 345 is shown for the date 2/12/80. The filled circles represent the flux density at each frequency while the filled triangles represent the energy at each frequency. The dotted lines are linear extrapolations of the infrared and radio data. Their intersection is used to estimate the turnover frequency. Impey and Neugebauer's (1988) data suggest the turnover occurs around 10^{12} while the work of Bregman puts the turnover frequency around 10^{11} Hz. The data presented here indicate a turnover frequency of $10^{11.2}$ Hz. The multifrequency data for 8/27/79 are shown as open circles.

The best fit parameters for each spectrum are compared in the first half of the following tables. A letter (first column) is assigned to each spectrum whose date is given in column 2. The third column gives the turnover frequency in Hz, the fourth the turnover flux density in cgs units and the fifth column gives the break frequency in Hz. The sixth column gives the optically thin spectral index and the seventh column the Compton flux density at 2 KeV. The Compton flux is in cgs units, i.e. ergs/cm^2-sec^{-1}-Hz^{-1}. The eighth column lists the distance to the source in gigaparsecs and the ninth column gives the angular diameter in milliarcseconds as determined from the variability timescale.

The second half of the tables list the results of equations 4-10 through 4-12 for the input parameters. The first column identifies the spectrum, the second gives time delay between the x-ray and optical observations, the third column lists the turnover frequency in Hz, and the fourth lists the Doppler boosting factor necessary to make the Compton flux equal the observed 2 KeV x-ray flux. The fifth column gives the magnetic field in Gauss and the sixth column the electron density at f^{A} in #/cm^{-3}. The last column gives the radius of the emitting region in parsecs. All quantities are in the rest frame of the source.

A second Table is presented for each source which shows the range of δ, B, N_0, and r for different values of the turnover frequency consistent with the observations.

0235+164 MODELS

Table 22 gives the input parameters and results for 0235+164

TABLE 22.
BEST FIT MODELS FOR 0235+164

INPUT PARAMETERS

	Date	Log ν_A	Log F_A	Log ν_b	α	log F^{SC}	θ	θ_0
A	2/1/80	10.9	-22.5	14.7	0.66	-29.4	7.46	6.3×10^{-6}
B	7/22/80	10.8	-22.5	14.7	0.65	-29.4	7.46	6.3×10^{-6}
C	7/29/80	10.7	-22.5	14.7	0.65	-29.7	7.46	6.3×10^{-6}
D	8/4/80	10.8	-22.2	14.7	0.65	-29.4	7.46	6.3×10^{-6}
E	8/5/80	10.8	-22.6	14.7	0.65	-29.4	7.46	6.3×10^{-6}
F	2/15/81	11.7	-22.8	14.7	0.97	-29.8	7.46	6.3×10^{-6}

MODEL RESULTS

Spectrum	dt (days)	log ν_A	δ	B (Gauss)	N^A (cm^{-3})	r (pcs)
A	4	10.9	38.0	0.02	0.68	0.6
B	0	10.8	42.0	0.01	0.57	0.4
C	3	10.7	44.0	0.01	0.34	0.4
D	14	10.8	46.0	0.02	0.27	0.2
E	15	10.8	39.0	0.01	0.60	0.4
F	20	11.7	18.5	0.70	0.43	0.08

Table 22 gives the SSC modelling results for 0235+164 if the size of the emitting region can be deduced from the most rapid variation. It should be noted that the Doppler factor is extremely sensitive to this size estimate. For instance, if the variability timescale increased by a factor of 10, the resulting Doppler factors would be a factor of 5 lower. The results indicate that relativistic beaming is needed with Doppler factors on the order of 40 for all but the last spectrum. The last spectrum, spectrum F, requires less beaming and a higher magnetic field than the other spectra. The difference occurs because the increase in brightness of the optical portion of the spectrum alters drastically the location of the turnover frequency. Any physical interpretation of this difference requires a more accurate method of estimating the turnover frequency. The range of allowable turnover frequencies for each observation and the resulting model parameters are listed for 0235+164 in Table 23. These results illustrate the range of allowable sizes, magnetic fields strengths, densities and Doppler factors. What we can conclude is that 0235+164 is beamed with a Doppler factor of at least 30 and is probably less than two parsecs in diameter.

TABLE 23.
MODELS FOR 0235+164

MODEL RESULTS

Spectrum	$\log f_A$	δ	B (Gauss)	N_A (cm^{-3})	r (pcs)
A	10.2-11.5	62-24	0.001-0.43	0.4-1.9	1.5-0.25
B	10.5-11.5	51-24	0.003-0.46	0.3-1.6	0.6-0.14
C	10.5-11.5	52-25	0.004-0.55	0.2-0.9	0.6-0.15
D	10.5-11.5	58-28	0.003-0.47	0.2-0.06	0.7-0.18
E	10.5-12.0	50-35	0.003-0.04	0.3-0.8	0.6-0.30
F	11.0-12.0	31-15	0.02-3.2	1.7-6.7	0.2-0.05

0735+17 MODELS

The best fit parameters and results for 0735+17 are listed in Table 24. The variability timescale gives an angular size of 9.1×10^{-5} milliarcseconds and the break frequency is estimated at $10^{14.75}$ Hz

TABLE 24.
BEST FIT MODELS FOR 0735+17

INPUT PARAMETERS

	Date	Log f_A	Log F_A	Log f_b	α	log F^{SC}	D	θ_0
A	4/18/79	11.5	-22.8	14.75	0.82	-29.7	2.74	9.1×10^{-5}
B	10/17/79	11.5	-22.9	14.75	0.77	-29.9	2.74	9.1×10^{-5}
C	3/31/80	11.5	-22.8	14.75	0.77	-29.9	2.74	9.1×10^{-5}
D	10/19/80	12.7	-23.6	14.75	0.73	-29.6	2.74	9.1×10^{-5}
E	3/26/81	12.7	-23.6	14.75	0.79	-29.8	2.74	9.1×10^{-5}

MODEL RESULTS

Spectrum	dt (days)	log f_A	δ	B (Gauss)	N_A (cm^{-3})	r (pcs)
A	9	11.5	7.9	1.5	5.0	0.08
B	20	11.5	7.4	2.4	5.0	0.07
C	12	11.5	7.7	2.0	5.0	0.07
D	0	12.7	5.3	200.0	200.0	0.003
E	0	12.7	2.0	547.0	290.0	0.005

Table 25 lists the model results for the allowable range of turnover frequencies.

TABLE 25.
MODELS FOR 0735+17

MODEL RESULTS

Spectrum	log f_A	δ	B (Gauss)	N_A (cm^{-3})	r (pcs)
A	11-12	11.5-5.5	0.13-1.5	2.5-11.0	0.2-0.04
B	11-12	11.5-5.3	0.16-2.4	2.0-10.0	0.2-0.03
C	11.5	7.7	2	4.6	0.07
D	12.7	5.3	200	240.0	0.003
E	12-13.0	3.6-1.7	17-2400	9000-485	0.02-0.004

The above results indicate a relatively modest amount of beaming is necessary to assure the Compton flux is consistent with the x-ray observations. Models D and E require large magnetic fields and small volumes because of the large the turnover frequency. Bregman et al. (1984) fit similar SSC models to their multifrequency observations of 0735+17. Their results agree well with the values presented above for turnover frequencies between $10^{10.7}$ and $10^{12.7}$ Hz.

OJ 287 MODELS

The modelling results for OJ 287 are given in Table 26. The minimum variability timescale indicates an angular radius θ_0 of 6×10^{-5} is appropriate for this source.

TABLE 26.
BEST FIT MODELS FOR OJ 287

INPUT PARAMETERS

Date	Log f_A	Log F_A	Log f_b	α	log F^{SC}	0	θ_0
A 10/26/79	11.4	-21.6	15.50	1.16	-29.2	1.9	5.9×10^{-5}
B 10/17/79	11.7	-21.9	15.50	1.18	-29.9	1.9	5.9×10^{-5}

MODEL RESULTS

Spectrum	dT (days)	log f_A	δ	B (Gauss)	N_{A_3} (cm^{-3})	r (pcs)
A	150	11.4	17.8	0.32	0.95	0.17
B	2	11.7	12.8	2.30	1.7	0.08

Table 27 shows the variation in the derived source parameters obtained by varying the turnover frequency.

TABLE 27.
MODELS FOR OJ 287

MODEL RESULTS

Spectrum	log f_A	δ	B (Gauss)	N_A (cm^{-3})	r (pcs)
A	11-12	19-9.5	0.04-6.6	1.0-1.7	0.2-0.05
B	11-12	20-10	10.5-10.5	0.7-1.3	0.2-0.05

The two multifrequency observations of OJ 287 analyzed above give similar results for all of the SSC parameters. Doppler boost factors on the order of 10 to 20 are necessary for the model to be consistent with the x-ray observations.

3C 273 MODELS

The modelling results for 3C 273 are shown in Table 28. The minimum variability timescale indicates the angular size of the emitting region is about 0.003 milliarcseconds. The break frequency must occur at frequencies beyond 10^{16} Hz.

TABLE 28.
BEST FIT MODELS FOR 3C 273

INPUT PARAMETERS

	Data	Log f_A	Log F_A	Log f_b	α	log F^{SC}	D	θ_e
A	12/13/78	11.6	-21.8	16.00	0.85	-28.1	0.92	8.0×10^{-3}
B	6/20/79	12.2	-22.5	16.00	0.82	-28.3	0.92	8.0×10^{-3}
C	1/ 1/80	12.4	-22.5	16.00	0.83	-28.3	0.92	8.0×10^{-3}
D	12/13/80	11.6	-21.8	16.00	0.87	-28.1	0.92	8.0×10^{-3}

TABLE 28--CONTINUED

MODEL RESULTS

Spectrum	dT (days)	log f_A	δ	B (Gauss)	N_{A_0} (cm^{-3})	r (pcs)
A	3	11.6	2.9	4.9	1.0×10^4	0.11
B	0	12.2	1.3	95.8	2.0×10^4	0.02
C	23	12.4	1.2	275.0	1.0×10^4	0.02
D	21	11.6	2.7	6.2	1.0×10^4	0.10

The results for 3C 273 indicate little if any beaming is necessary to satisfy the x-ray observations. The magnetic field predicted for spectrum C is two order of magnitudes greater than predicted for spectra A and D. The physical sizes of the emission regions are all less than 0.1 parsec. Table 29 lists the variations of the derived source parameters with the turnover frequency for 3C 273. In the realistic limits, the parameters derived from all of the multifrequency spectra of 3C 273 are consistent with a model with a Doppler factor of 2, a magnetic field of 10-20 Gauss and a emitting region of less than a tenth of a parsec.

TABLE 29.
MODELS FOR 3C 273

MODEL RESULTS

Spectrum	log f_A	δ	B (Gauss)	N_{A_0} (cm^{-3})	r (pcs)
A	11.5-12	3-2	3-43	$1.4\text{-}1.3 \times 10^4$	0.1-0.06
B	11.5-12	2-1	3-45	$2.0\text{-}1.6 \times 10^3$	0.1-0.03
C	11.5-12	2.2-1.5	3-37	$2.0\text{-}1.0 \times 10^4$	0.1-0.03
D	11.5-12	3.2	3-40	$2.0\text{-}1.0 \times 10^4$	0.1-0.06

AP LIBRAE MODELS

Results for the SSC models of AP Librae are shown in Table 30. An angular size of 0.008 milliarcseconds was determined from RHO optical variability data. The sharp break in the optical spectrum is interpreted as the break frequency for the SSC models. Table 31 gives the variation of the derived source parameters with variation of the turnover frequency.

TABLE 30.
BEST FIT MODELS FOR AP LIBRAE

INPUT PARAMETERS

	Date	Log f_A	Log F_A	Log f_b	α	log F^{SC}	D	θ_0
A	2/26/79	12.0	-22.8	14.80	0.80	-29.7	0.27	3.0×10^{-3}
B	8/ 3/79	12.0	-22.8	14.80	0.80	-31.0	0.27	3.0×10^{-3}
C	2/10/81	11.9	-22.8	14.80	0.71	-29.8	0.27	3.0×10^{-3}
D	2/ 8/81	11.9	-22.8	14.80	0.71	-29.7	0.27	3.0×10^{-3}

MODEL RESULTS

Spectrum	dt (days)	log f_A	δ	B (Gauss)	N_0 (cm^{-3})	r (pc)
A	30	12.0	1.0	204	3.0×10^{4}	0.01
B	8	12.0	1.0	623	4.0×10^{4}	0.01
C	1	11.9	1.0	183	2.0×10^{4}	0.01
D	4	11.9	1.0	150	2.0×10^{4}	0.01

TABLE 31.
MODELS FOR AP LIBRAE

MODEL RESULTS

Spectrum	log ν_A	δ	B (Gauss)	N_A (cm^{-3})	r (pcs)
A	11.5-12.0	1.4-1	18-214	$7.0-6.0x10^4$	0.03-0.006
B	11.5-12.5	1.5-0.8	56-8270	$6.0-5.0x10^4$	0.03-0.006
C	11.5-12.5	1.4-0.7	26-3790	$3.0-3.5x10^4$	0.02-0.005
D	11.5-12.0	1.4-0.7	25-3600	$3.0-3.1x1^{-4}$	0.02-0.05

All of the models in Table 30 require no relativistic beaming. The models in Table 31 that show a small amount of beaming is consistent with a low frequency turnover, while for high frequency turnover models the x-ray flux is actually too large. On this basis we can restrict the turnover frequency to lie at frequencies below 10^{12} Hz.

3C 345

Models for the four multifrequency spectra of 3C 345 are shown in Tables 32 and 33. The variability timescale derived from RHO observations indicated the emission region was smaller than $3.6x10^{-5}$ milliarcseconds.

TABLE 32.
BEST FIT MODELS FOR 3C 345

INPUT PARAMETERS

	Date	Log ν_A	Log F_A	Log ν_b	α	log F^{SC}	D	θ_e
A	8/27/79	11.3	-21.8	16.00	1.18	-29.6	4.17	$3.6x10^{-5}$
B	1/24/80	11.2	-21.6	16.00	1.12	-29.6	4.17	$3.6x10^{-5}$
C	2/12/80	11.1	-21.6	16.00	1.12	-29.5	4.17	$3.6x10^{-5}$
D	8/18/80	10.8	-21.6	16.00	0.97	-29.5	4.17	$3.6x10^{-5}$

TABLE 32 -CONTINUED.

MODEL RESULTS

Spectrum	dt (days)	log f_A	δ	B (Gauss)	N_A (cm^{-3})	r (pcs)
A	12	11.3	22	0.15	8.0×10^5	0.38
B	78	11.2	27	0.10	4.0×10^6	0.52
C	60	11.1	28	0.07	5.0×10^6	0.60
D	12	10.8	34	0.02	4.0×10^5	0.86

TABLE 33.
MODELS FOR 3C 345

MODEL RESULTS

Spectrum	log f_A	δ	B (Gauss)	N_A (cm^{-3})	r (pcs)
A	11-12	27-13	0.04-6.5	$6.0\text{-}3.0 \times 10^5$	0.54-0.13
B	11-12	30-15	0.05-7.2	$2.0\text{-}5.0 \times 10^6$	0.65-0.16
C	11-12	30-15	0.04-7.0	$6.0\text{-}2.0 \times 10^6$	0.70-0.16
D	11-12	30-14	0.06-9.0	$5.0\text{-}4.0 \times 10^5$	0.64-0.15

The results for 3C 345 indicate all of the observations are consistent with a source with a radius of half a parsec and a magnetic field strength of about 0.1 Gauss. The radiation is beamed with a Doppler boost factor of about 27. Bregman *et al.* (1986) derived magnetic fields on the order of 2.0 Gauss, Doppler boosting factor on the order of 3, and the radius of the emitting region of 0.5 parsec. The Doppler boosting factors derived here are larger than the one derived by Bregman *et al.* by a factor of 10. These differences probably arise because the x-ray data used for the Bregman *et al.* spectrum were made two years before the other multifrequency observations and are not truly simultaneous.

CONCLUSIONS

We have analyzed the nearly simultaneous x-ray and optical data for six of the sources in the individual source list in terms of the synchrotron self-Compton model. We assumed the infrared emission is optically thin synchrotron radiation. The observed x-ray emission is considered to be self-Compton emission from the synchrotron source. The input parameters for the SSC models are deduced from the multifrequency spectrum for each source. Physical characteristics of the emission region as calculated from the SSC models for each individual spectrum are compared with the other spectra of that object. Models are calculated for a range of turnover frequencies since the SSC models are especially sensitive to changes in this parameter, and because the turnover occurs in a region devoid of observations. Four of the sources, 0235+164, 0735+17, OJ 287, and 3C 345, require relativistic motion to avoid the "Compton catastrophe". Neither 3C 273 nor AP Librae require bulk relativistic motion, but small boosting factors are consistent with the data. The magnetic field strengths are typically a few tenths of a Gauss to several Gauss with the exception of AP Librae. This Lacertid requires magnetic fields between 15 and 4800 Gauss. The latter value is unrealistically large. If we restrict the magnetic field strength to values below a few hundred Gauss, we can restrict the synchrotron turnover frequency to be below 10^{12} Hz.

The diameter of the emission region is determined by the angular sizes and the Doppler boosting factors. The diameters of the sources fall in a range between 0.05 and 0.7 parsecs in the source rest frame

These diameter estimates are similar to the sizes found in other multifrequency studies

CHAPTER V
CONCLUSIONS

The data in this dissertation represent a significant attempt to analyze seventy nearly simultaneous x-ray and optical observations carefully and consistently. The assorted sample of thirty six sources for which observations were obtained include non-optically violent variable AGN, OVV quasars, BL Lac type sources and Seyfert galaxies.

Nine of the fifteen high count rate IPC observations required hydrogen column densities exceeding the galactic column densities in the directions of the sources. The errors in the fitted column densities were large, so further work needs to be done in this area. The BBXRT x-ray spectrometer should be able to resolve many of the fundamental questions concerning the x-ray spectra of AGNs, including the intrinsic column density problem.

A number of sources studied in this work had more than one nearly simultaneous x-ray and optical observation. The x-ray and optical flux curves of these sources were compared in an effort to gain insight into the connection between the x-ray emission and the optical emission. An x-ray flare seen in 0235+164 preceded an optical flare by about 100 days. X-ray variability was seen in four of the six BL Lacertids, in three of the four quasars, and in the one Seyfert galaxy. The proposed X-ray Timing Explorer (XTE) will be able to examine more closely the x-ray variability characteristics of these sources. Study of the relationship between x-ray flares and optical flares will require a great deal of cooperation between ground-based observers and satellite observers, as have the past multifrequency campaigns.

A sophisticated least squares routine which accounts for errors in both the independent and dependent variables was used to determine the relationship between the x-ray luminosity and the optical luminosity. The results indicate that optical luminosity is proportional to the x-ray luminosity ($L_o = L_x^b$, $b = 1$), the probability of this correlation occurring by chance is 4×10^{-8}. The luminosities of the non-optically violent variable sources are highly correlated with $b = 1.09$. The class of AGN which exhibits optically violent behavior, the blazars, were much less correlated than the non-OVV's. They exhibited a b of 0.88 and a probability that this correlation could arise by chance of 1×10^{-5}. The x-ray and optical spectral indices for BL Lacertids were steeper than for quasars, a result which has been found in other studies.

Correlations of the luminosity ratio, L_x/L_o, with optical luminosity and with redshift were both inconclusive. Indications that if a correlation exists between the luminosity ratio and the optical luminosity, it is an inverse correlation. The redshift distribution in the sample analyzed here was not sufficient to draw any conclusions about the variation of the luminosity ratio with redshift. Further studies of this type with more high redshift sources are necessary to realistically address this question.

Six of the sources with multiple x-ray observations were observed by the IRAS infrared satellite. These IRAS data, combined with radio observations made contemporaneously with the x-ray and optical observations, were used to construct multifrequency spectra of the six sources. The synchrotron-self-Compton model of Jones, O'Dell and Stein (1974) was used to model these multifrequency spectra and estimate physical conditions in each source. The lack of data in near the synchrotron self-absorption (turnover) frequency prevented accurate modelling. The various parameters are highly dependent on this frequency. Several models for each spectrum were run, varying the turnover frequencies within the range allowed by the observations.

Five of the six spectra of 0235+164 required relativistic beaming with Doppler boost factors of 20-60, the remaining one required smaller boost factors in the range of 15-30, depending on the choice of the turnover frequency. The magnetic field strength of 0235+164 ranged from 0.0006 to 3 Gauss and the physical radius was on the order of 0.3 to 1.5 parsecs.

Three of the five 0735+17 spectra were consistent with a source of radius 0.05 to 0.2 parsec containing a 0.1-200 Gauss magnetic field and a Doppler boost factor of seven. The two other spectra required stronger magnetic fields, 17-2400 Gauss and slightly smaller boost factors on the order of 2-5.

The two OJ 287 spectra were consistent with a model of radius 0.05-0.23 parsec and magnetic field strengths of 0.04-6.0 Gauss. The Doppler boost factors ranged from 10 to 20.

The spectra of 3C 273 required no Doppler boosting, but the magnetic field strengths were large, 3.0 to 40.0 Gauss. The radius of the emitting region is between 0.03 and 0.1 parsec.

AP Librae also required no Doppler boosting, but required excessive magnetic field strengths between 10 and 4800 Gauss. In order to restrict the magnetic fields to reasonable values, the turnover frequency cannot exceed 10^{12} Hz. The radius of the emitting region is between 0.004 and 0.03 parsec.

Models of 3C 345 are consistent with a source 0.13-0.7 parsec in radius, containing a moderate magnetic field of 0.04-9.0 Gauss and having Doppler boost factors on the order of 15-30.

The dependence of the Doppler boost factor and the magnetic field strength on the turnover frequency requires accurate knowledge of the location of the turnover before models can be reasonably constrained. Observations between 10^{10} and 10^{12} Hz are critical to multifrequency analysis. Improvement in establishing the optically thin spectral index requires simultaneous far-infrared, near-infrared, and optical observation along with a measurement of the self-Compton flux in the x-ray band. The possibility that the x-ray emission is a combination of the Compton flux plus other components is indicated by the difference in the x-ray spectral index and the infrared spectral index. The BBXRT might help distinguish between these x-ray components.

BIBLIOGRAPHY

Alfven, A. and Herlofsen, N. 1950, Phys. Rev., 78, 616.

Allen, D. A., Ward, M. J., and Hyland, A. R. 1982, M.N.R.A.S., 199, 969.

Aller, H. D., Aller, M. F., Latimer, G. E. and Hodge, P. E. 1985, Ap. J. Supp., 59, 513.

Arp, H. C. 1987, Quasars, Redshifts and Controversies (Berkeley: Interstellar Media).

Avni, Y. 1976, Ap. J., 210, 642.

Avni, Y., and Tananbaum, H. 1986, 305, 83.

Begelman, M. C., Blandford, R. D. and Rees M. 1984, Rev. Mod. Phys., 56, 255.

Bevington, P. R. 1969, Data Reduction and Error Analysis for the Physical Sciences (New York: McGraw Hill Book Co.).

Blandford, R. D. and Znajek, R. L. 1977, M.N.R.A.S., 179, 433.

Blumenthal, G. R. and Gould, R. J. 1970, Rev. Mod. Phys., 42, 237.

Blumenthal, G. R., Keel, W. C., and Miller, J. S. 1982, Ap. J., 257, 499.

Boldt, E. and Leiter, D., Ap. J., 276, 427.

Boroson, T. A., Oke, J. B. and Green, R. F. 1982, Ap. J., 263, 32.

Bradt, H. V., Doxsey, R. E., Johnston, M. D., Schwartz, D. A., Burkhead, M. S., Dent, W. A., Liller, W., and Smith, A. G. 1979, Ap. J., 230, L5.

Bregman, J. N., Lebofsky, M. J., Aller, M. F., Rieke, G. H., Aller, H. D., Hodge, P. E., Glassgold, A. E. and Huggins, P. J. 1981, Nature, 293, 29.

Bregman, J. N., Glassgold, A. E., Huggins, P. J., Aller, H. D., Aller, M. F., Hodge, P. E., Rieke, G. H., Lebofsky, M. J., Pollock, J. T., Pica, A. J., Leacock, R. J., Smith, A. G., Webb, J., Balonek, T. J., Dent, W. A., O'Dea, C. P., Ku, W. H.-M., Schwartz, D. A., Miller, J. S., Rudy, R. J. and Levan, P. D. 1984, Ap. J., 276, 454.

Bregman, J. N., Glassgold, A. E., Huggins, P. J., Neugebauer, G., Soifer, B. T., Matthews, K., Elias, J., Webb, J., Pollock, J. T., Pica, A. J., Leacock, R. J., Smith, A. G., Aller, H. D., Aller, M. F., Hodge, P. E., Dent, W. A., Balonek, T. J., Barvainis, R. E., Roellig, T. P. L., Wisniewski, W. Z., Rieke, G. H., Lebofsky, M. J., Wills, B. J., Wills, D., Ku, W. H. M., Bregman, J. D., Witteborn, F. C., Lester, D. F., Impey, C. D., and Hackwell, J. A. 1986b, Ap. J., 301, 708.

Bregman, J. N., Glassgold, A. E., Huggins, P. J., and Kinney, A. L. 1986a, Ap. J., 301, 698.

Bregman, J. N., Glassgold, A. E., Huggins, P. J., Kinney, A. L., McHardy, I., Webb, J. R., Pollock, J. T., Leacock, R. L., Smith, A. G., Pica, A. J., Aller, H. D., Aller, M. F., Hodge, P. E., Miller, J. S., Stevens, S. A., Dent, W. A., Balonek, T. J., Barvainis, R., Neugebauer, G., Impey, C. D., Soifer, B. T., Matthews, K., Elias, J. H., and Wisniewski, W. Z. 1988, In press in Ap. J.

Brown, L. M. J., Robson, E. I., Gear, W. K., Hughes, D. H., Griffin, M. J., Geldzahler, B. J., Schwartz, P. R., Smith, A. G., Smith, M. G., Shepherd, D. W., Webb, J. R., Valtaoja, E., Terasranta, H., and Salonen, E. 1988, pre-print.

Burbidge, G. 1980, *Objects of High Redshift*, ed. G. O. Abell and P. J. E. Peebles (Dordrecht: D. Reidel Publishing Co.), p. 99.

Burstein, D., and Heiles, C. 1978, Ap. J., 225, 40.

Burstein, D., and Heiles, C. 1982, A. J., 87, 1165.

Chanan, G. A. 1983, Ap. J., 275, 45.

De Zotti, G., Boldt, E. A., Cavaliere, A., Danese, L., Franceschini, A., Marshall, F. E., Swank, J. H., and Szymkowiak, A. E. 1982, Ap. J., 253, 47.

Elvis, M., Green, R. F., Bechtold, J., Schmidt, M., Neugebauer, G., Soifer, B. T., Matthews, K., and Fabbiano, G. 1986, Ap. J., 310, 291.

Elvis, M., and Lawrence, A. 1985, *Astrophysics of Active Galaxies and Quasi-Stellar Objects*, edited by J. S. Miller (Mill Valley, Ca.: University Science Books).

Giacconi, R., Branduardi, G., Briel, U., Epstein, A., Fabricant, D., Feigelson, E., Forman, W., Gorenstein, P., Grindlay, J., Gursky, H., Harnden, Jr., F. R., Henry, J. P., Jones, C., Kellogg, E., Koch, D., Murray, S., Schreier, E., Seward, F., Tananbaum, H., Topka, K., Van Speybroeck, L., Holt, S. S., Becker, R. H., Boldt, E. A., Serlemitsos, P. J., Clark, G., Canizares, C., Markert, T., Novick

R., Helfand, D., and Long, K., 1979, Ap. J., 230, 540.

Giacconi, R., Gursky, H., Paolini, F., and Rossi, B. 1962, Phys. Rev. Lett., 9, 439.

Gorenstein, P., Harnden, F. R. Jr., and Fabricant, D. G., 1978, IEEE Trans., NS-25, 869.

Hewitt, A. and Burbidge, G. 1987, Ap. J. Supp., 63, 1.

Impey, C. D. and Neugebauer, G. 1988, A. J., 95, 307.

Jefferys, W. H. 1980, A. J., 85, 177.

Johnson, H. L. 1966, Ann. Rev. Astron. Ap., 4, 193.

Jones, T. W., O'Dell, S. L. and Stein, W. A. 1974, Ap. J. 188, 353.

Jones, T. W., Rudnick, L. and Landau, R. 1986, *Continuum Emission of Active Galactic Nuclei* (Tucson: NOAO).

Kellogg, E., Henry, P., Murray, S., Van Speybroeck, L., and Bjorkholm, P. 1976, Rev. Sci. Instr., 47, 282.

Kriss, G. A., Canizares, C. R., and Ricker, G. R., 1980, Ap. J., 242, 492.

Ku, W. H.-M., Helfand, D. J., and Lucy, L. B. 1980, Nature, 288, 323.

Landau, R., Golisch, B., Jones, T. J., Jones, T. W., Pedelty, J., Rudnick, L., Sitko, M. L., Kenney, J., Roellig, T., Salonen, E., Urpo, S., Schmidt, G., Neugebauer, G., Matthews, K., Elias, J. H., Impey, C., Clegg, P. and Harris, S. 1986, Ap. J., 308, 78.

Lu, P. K. 1972, A. J., 77, 829.

MacAlpine, G. M. 1985, *Astrophysics of Active Galaxies and Quasi-Stellar Objects*, ed. J. S. Miller (Mill Valley: University Science Books), p. 259.

Madejski, G. M., and Schwartz, D. A. 1988, in Press in Ap. J.

Marshall, N., Warwick, R. S., and Pounds, K. A. 1981, M.N.R.A.S., 194, 987.

Matthews, T. A. and Sandage, A. 1963, Ap. J., 138, 30.

McHardy, I. 1985, Space Science Reviews, 40, 560.

Mushotzky, R. F. 1982, Ap. J., 256, 92.

Mushotzky, R. F., and Marshall, F. E. 1980, Ap. J., 239, L5.

Mushotzky, R. F., Marshall, F. E., Boldt, E. A., Holt, S. S., and Serlemitsos, P. J. 1980, Ap. J., 235, 377.

O'Dell, S. L., Puschell, J. J. and Stein, W. A. 1977, Ap. J., 213, 351.

O'Dell, S. L., Puschell, J. J., Stein, W. A. and Warner, J. W. 1978, Ap. J. Supp., 38, 267.

Pica, A. J. 1982. Optical and Radio Properties of QSOs as a Function of Absolute Luminosity, Ph. D. Dissertation, The University of Florida.

Pica, A. J., Pollock, J. T., Smith, A. G., Leacock, R. J., Edwards, P. L., and Scott, R. L. 1980, A. J., 85, 1442.

Pica, A. J., Webb, J. R., Smith, A. G., Leacock, R. J., and Bitran, M. 1987, A. J., 94, 289.

Pollock, J. T. 1982. The Morphology and Energetics of Discrete Optical Events in Compact Extragalactic Objects. Ph. D. Dissertation. The University of Florida.

Schmidt, M. 1968. Ap. J., 151, 393.

Schmidt, M., and Green, R. F. 1983, Ap. J., 269, 352.

Schmidt, M., and Green, R. F. 1986. Ap. J., 305, 68.

Seaton, M. J. 1979, M.N.R.A.S., 187, 73.

Schrier, E. J. 1978. New Instrumentation for Space Astronomy (New York: Pergamon Press).

Schwartz, D. A., and Ku, W. H.-M., 1983. Ap. J., 266, 459.

Smith, P. S. 1986, Polarimetry and Photometry of Active Quasars at Visual and Near Infrared Wavelengths, Ph. D. Dissertation. University of New Mexico.

Stark, A. A., Heiles, C., Bally, J., and Linke, R. 1988, in preparation.

Tananbaum, H., Avni, Y., Branduardi, G., Elvis, M., Fabbiano, G., Feigelstein, E., Giacconi, R., Henry, J. P., Soltan, A., and Zamorani, G. 1979 Ap. J., 234, L9-L13.

Tananbaum, H., Avni, Y., Green, R., Schmidt, M., and Zamorani, G. 1986, Ap. J., 305, 57.

Tananbaum, H., Wardle, J. F. C., Zamorani, G., and Avni, Y. 1983, Ap. J., 268, 60.

Tucker, W. H. 1983, Ap. J., 271, 531.

Urry, C. M. 1984, X-Ray and Ultraviolet Observations of BL Lacertae Objects, Ph. D. Dissertation, The Johns Hopkins University.

Urry, C. M. 1988, preprint.

Van Speybroeck, L. P. 1977, SPIE Proc., 106, 136.

Webb, J. R. 1985, Effects of Optical Variability on X-Ray-Optical Correlations, Ms. Thesis, The University of Florida.

Webb, J. R., and McHardy, I. 1986, Continuum Emission of Active Galactic Nuclei, ed. M. Sitko, (Tucson: NOAO).

Webb, J. R., Smith, A. G., Leacock, R. J., Fitzgibbons, G. L., Gombola, P. P., and Shepherd, D. W. 1988, A. J., 95, 374.

Weedman, D. W. 1988, Quasar Astronomy, (Cambridge: Cambridge University Press).

Wilkes, B. and Elvis, M. 1986, Continuum Emission of Active Galactic Nuclei (Tucson: NOAO).

Worrall, D. M. 1986, Continuum Emission of Active Galactic Nuclei (Tucson: NOAO).

Worrall, D. M., Mushotzky, R. F., Boldt, E. A., Holt, S. S., and Serlemitsos, P. J. 1979, Ap. J., 232, 683.

Zamorani, G., Henry, J. P., Maccacaro, T., Tananbaum, H., Soltan, A., Avni, Y., Liebert, J., Stock, J., Strittmatter, P. A., Weymann, R. J., Smith, M. G., and Condon, J. J., 1981, Ap. J., 245, 357.

APPENDIX
X-RAY SPECTRA

The x-ray spectra of the fifteen sources whose count rates were sufficient to obtain reliable spectral fits are shown. All fits are power laws with neutral hydrogen absorption added until an acceptably low chi-square value is obtained. The sources whose spectra are included in this appendix are 0007+10, 0235+164, 3C 120, 0735+17, OJ 287, MRK 421, 3C 273, 3C 345, 3C 351 1727+50 OV-236 2135-14, 2155-30 and 2200+42

The plots were reproduced from the FINSPEC output at the Smithsonian Center for Astrophysics in Cambridge Massachusetts FINSPEC is the reduction program which fits the model (in this case a power law) to the detector response function and the observed counts

The bottom plot shows the log of the observed counts (observed spectrum) in each of the 14 energy bins between 0.1 and 8.0 KeV. Usually 10 or 12 of the center bins were used for fitting, because of uncertainties in determining the counts in the outer bins The upper plot shows the spectrum of incident x-rays which, if the linear model is correct, gives the observed spectrum when folded with the detector response

These spectra were used to obtain the spectral indices in Table 3 and the hydrogen column densities quoted in Chapter 2

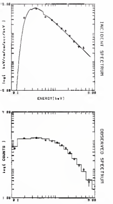

FIGURE A1. The x-ray spectrum of 0007+10. A spectral index of 1.5 and a column density of 3.162×10^{20} resulted in a minimum chi square value of 16.1.

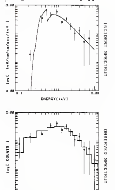

FIGURE A2 The x-ray spectrum of 3C 66A The spectral index is 1.63 and the best fit hydrogen column density is 1.778x10^{21} These parameters yielded a minimum chi-square value of 7.5.

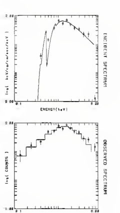

FIGURE A3 The x-ray spectrum of 3C 120 The best fit spectral index was 1 38 with a hydrogen column of $1x10^{21}$ These parameters yielded a minimum chi-square value of 9 0

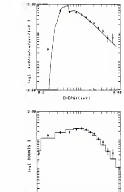

FIGURE A4. The x-ray spectrum of 0735+17. The best fit spectrum shown above has a spectral index of 1.5 and a hydrogen column density of 1.0x10^{21}. The resulting chi-square for the fit was 14.9

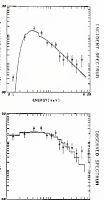

FIGURE A5 The x-ray spectrum of OJ 287 The fit is characterized by a spectral index of 1.5 and a column density of 3.16×10^{20} The minimum chi-square value was 10.9

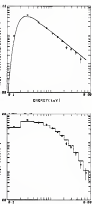

FIGURE A6. The x-ray spectrum of MRK 421 is shown. The spectral index is 1.25 and the column density is 1.77×10^{20}. the minimum chi-square value was 22.2.

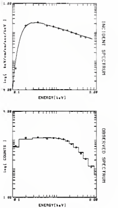

FIGURE A7 The x-ray spectrum of 3C 273. The best fit spectral parameters were: spectral index = 0.5; hydrogen column density = 1.0×10^{20}.

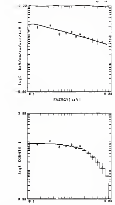

FIGURE A8 The x-ray Spectrum of 3C 345. The spectral index is 0.40 and the column density is 1.05×10^{20}. The minimum chi-square value was 9.7.

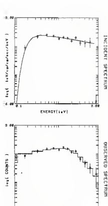

FIGURE A9 The x-ray spectrum of 3C 351. The best fit spectral index was 0.28 and the column density was 2.3×10^{20}. The chi-square value for the fit was 10.0.

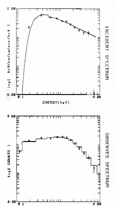

FIGURE A10 The x-ray spectrum of 1727+50 A power law with spectral index 0 75 and a hydrogen column density of 2 7x10^{20} gave a minimum chi-square value of 5 8

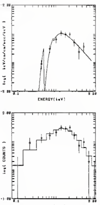

FIGURE A11 The x-ray spectrum of OV 236 The best fit power law had a spectral index of 1 81 and a hydrogen column of 7 489x10^{21} The minimum chi-square value was 6 3

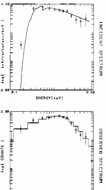

FIGURE A12 The x ray spectrum of 2128-12 The spectral index is 0.63 and the hydrogen column is 6.668×10^{20} The minimum chi-square value was 4.3.

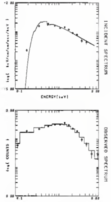

FIGURE A13. The x-ray spectrum of 2135-14. The spectral index is 0.88 and the hydrogen column is 5.47x10^{20}. The minimum chi square is 20.7

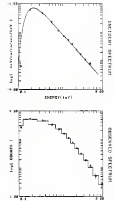

FIGURE A14 The x-ray spectrum of PKS 2155-30 The spectral index is 1.75 and the hydrogen column is 1.73x10^{20} The minimum chi-square value was 83.3

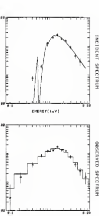

FIGURE A15 The x-ray spectrum of 2200+42 (BL LAC) The spectral index is 2.25 and the column density is 1.0×10^{22} The minimum chi-square value is 8.0

BIOGRAPHICAL SKETCH

James Raymond Webb was born in Anderson, Indiana on August 5, 1954. He graduated from Anderson High School in 1972. After working for several years, he decided to enroll in Ball State University, Muncie, Indiana at age 21. He worked full time in an General Motors factory and attended school part time until he received his Bachelor of Science in physics on July 11, 1980. He was then accepted by the University of Florida's Astronomy graduate program, where he worked first as a teaching assistant and then as a research assistant with the R.O.V.E.R. program. On May 4, 1985, he obtained his Master's degree in Astronomy at UF. During his graduate years he met and married fellow student Beatriz Fernandez, played many an inspired game of basketball and observed many, many quasars. On August 8, 1988, he was awarded a Ph. D. in Astronomy by the University of Florida, thus realizing a long strived-for ambition.

I certify that I have read this study and that in my opinion it conforms to acceptable standards of scholarly presentation and is fully adequate, in scope and quality, as a dissertation for the degree of Doctor of Philosophy.

A. G. Smith, Chairman
Distinguished Service Professor of Astronomy

I certify that I have read this study and that in my opinion it conforms to acceptable standards of scholarly presentation and is fully adequate, in scope and quality, as a dissertation for the degree of Doctor of Philosophy.

James H. Hunter

James H. Hunter
Professor of Astronomy

I certify that I have read this study and that in my opinion it conforms to acceptable standards of scholarly presentation and is fully adequate, in scope and quality, as a dissertation for the degree of Doctor of Philosophy.

Haywood C. Smith Jr.

Haywood C. Smith Jr.
Associate Professor of Astronomy

I certify that I have read this study and that in my opinion it conforms to acceptable standards of scholarly presentation and is fully adequate, in scope and quality, as a dissertation for the degree of Doctor of Philosophy.

James R. Ipser
Professor of Physics

I certify that I have read this study and that in my opinion it conforms to acceptable standards of scholarly presentation and is fully adequate, in scope and quality, as a dissertation for the degree of Doctor of Philosophy.

James N. Fry

James N Fry
Assistant Professor of Physics

I certify that I have read this study and that in my opinion it conforms to acceptable standards of scholarly presentation and is fully adequate, in scope and quality, as a dissertation for the degree of Doctor of Philosophy.

Gary G Ihas

Gary Ihas
Professor of Physics

This dissertation was submitted to the Graduate Faculty of the Department of Astronomy in the College of Liberal Arts and Sciences and to the Graduate School and was accepted in partial fulfillment of the requirements for the degree of Doctor of Philosophy

August 1988

Dean, Graduate School